Aggregation reduces the release of bioavailable silicon from allophane and phytolith

Zimin Li, Jean-Dominique Meunier, Bruno Delvaux

Aggregation reduces the release of bioavailable silicon from allophane and phytolith

Zimin Li[‡,*], Jean-Dominique Meunier[†], Bruno Delvaux[‡]

[‡] Earth and Life Institute, Soil Science, Université catholique de Louvain (UCLouvain), Croix du Sud 2, L7.05.10, 1348 Louvain-La-Neuve, Belgium.

[†] CNRS, CEREGE, Aix Marseille Université, 13545 Aix-en-Provence Cedex 04, France.

[*]**Corresponding author:** zimin.li@uclouvain.be (Zimin Li)

Address: Earth and Life Institute, Soil sciences, Université catholique de Louvain (UCLouvain), Croix du Sud 2 / L7.05.10, 1348 Louvain-la-Neuve, Belgium.

Submitted to the journal of ***Geochimica et Cosmochimica Acta***

Tables: **5**

Figures: **9**

Pages: **31**

Supporting information (S)

Abstract

Phytoliths form in plant tissues as fine, silt-sized amorphous silica particles. Once deposited in soils by plant debris, they can dissolve and feed silicon (Si) fluxes to the biosphere and hydrosphere, enhancing the positive effects of Si on plant health and carbon fixation by marine diatoms. In soils, microaggregates (<250 μm) may entrap phytoliths and protect them from dissolution. Here we aimed at analyzing the role of aggregation in protecting phytoliths and delaying the release of bioavailable Si. Synthetic 32-days aged aggregates were composed of (g kg^{-1}): organic matter (50), aluminosilicate mineral (370), iron (Fe) oxide (60), quartz (500) and rice phytolith (20). Models with either amorphous (*Am*) or crystalline (*Cryst*) aluminosilicates and Fe-oxides were tested. The *Am* model included allophane and ferrihydrite while the *Cryst* model included kaolinite and goethite. Aggregates were visualized by Scanning and Transmission Electron Microscopy. They were compared to individual compounds and unaggregated mixtures through kinetic Na_2CO_3 and $CaCl_2$ extraction assessing the pools of phytoliths and bioavailable Si, respectively. Aluminum (Al) and germanium (Ge) concentrations, and pH were measured in the $CaCl_2$ extracts. $CaCl_2$ extractable Si decreased in the order (g kg^{-1}): *Am* mixture (3.72) > *Am* aggregate (0.95) > *Cryst* mixture (0.48) > *Cryst* Aggregate (0.39). Aggregation thus reduced Si release by 3.9- and 1.2- fold in the amorphous and crystalline model, respectively. The Si/Al and Ge/Si atomic ratios showed that allophane and phytolith were the main sources of bioavailable Si in the amorphous and crystalline model, respectively. In contrast to the crystalline model (pH 5.0-7.8), the acidic medium in the amorphous model (pH 3.7-4.9) enhanced allophane dissolution. Aggregation thus protected both allophane and phytolith from dissolution, and reduced the release of bioavailable Si, the source of which depended on the component stability and pH.

Key words: aggregation, phytolith, allophane, bioavailable silicon.

Introduction

Ehrenberg (1846) described for the first-time plant silica bodies in many soils of the world, naming them *Phytolitharia*. Phytoliths are microscopic hydrated amorphous silica ($SiO_2.nH_2O$; opal-A) particles forming in living plants, which take up monosilicic acid (H_4SiO_4) from soil solution. The primary source of aqueous H_4SiO_4 in soils is silicate weathering (Erhart, 1963; Bartoli, 1983), which may consume carbon dioxide (CO_2) (Berner, 1997), depending on carbonic acid dissociation, hence pH. Phytoliths vary widely in shape and size, which ranges from 0.1 to 200 μm (Nawaz et al., 2019), thus encompassing silt- and fine sand-sized phytoliths (Piperno, 1988), as well as fine silt- and clay-sized biogenic silica particles (≤ 5μm) (Puppe et al., 2017). All phytoliths dissolve in water and dilute solutions at common pH values (4.5-8) of soil solution (Fraysse et al., 2006, 2009; Puppe et al., 2017). The dissolution rate of phytoliths is 10^2-10^4 higher than that of typical soil crystalline clay and parent-rock silicate minerals (Fraysse et al., 2009). Phytolith dissolution releases dissolved silicon (Si), which can follow four routes. It can be (i) taken up by plants, providing them vigor, disease regulation and tolerance to abiotic stresses (Epstein, 1994; Coskun et al., 2019); (ii) transferred to watersheds (Bartoli, 1983; Derry et al., 2005), hence contributing to the oceanic capacity to fix CO_2 since Si is an essential nutrient for diatoms (Erhart, 1963; Conley, 2002). Processes such as (iii) H_4SiO_4 adsorption on aluminum (Al) and iron (Fe) oxides (Jones and Handreck, 1963), and (iv) aluminosilicate neoformation (Cornelis and Delvaux, 2016; Li et al., 2020a), also remove DSi from soil solution. The soil-to-plant Si cycle thus strongly affects the global Si cycle (Erhart, 1963; Conley, 2002; Meunier, 2003). Also, it impacts plant health and crop performance (Epstein, 1994; Coskun et al., 2019). In turn, Si cycling is affected by land use, soil processes and properties (Bartoli, 1983; Cornelis and Delvaux, 2016; Li et al., 2019; Li et al., 2020b; Vandevenne et al., 2015; Vander Linden and Delvaux, 2020).

Aggregation is a natural soil process generating particle aggregates in which, for instance, organic carbon (OC) may be stabilized and protected (Six et al., 2002). This process involves primarily colloidal interactions (Sposito, 2016). It thus relies on the reactivity of soil components, which are basically related to their heterogeneity, fine size and charge properties (Johnston and Tombácz, 2002). Phytoliths extracted from plant materials have a specific surface area (SSA) reaching 92-315 $m^2\ g^{-1}$. They have a

pH at the isoelectric point (pH_{IEP}) between 0.9 and 2.2 (Fraysse et al., 2009), reflecting that the phytolith surface carries a negative charge at common soil solution pH values. In soils, chemisorption of hexacoordinated Al onto phytoliths affects its surface charge (Bartoli, 1985). Enhanced OM adsorption by Al (Bartoli, 1985) is a fundamental process in organo-mineral interactions that facilitates aggregation and OM preservation (Deng and Dixon, 2002). In this respect, Bartoli (1985) noted an average residence time of OM on soil phytoliths that was twice that on clay minerals, indicating a protective effect of the phytolith–$Al(OH)_n$–OM association against OM biodegradation. Soil microaggregates (<250 μm) may entrap individual phytoliths (Li et al, 2020b). Thereby, aggregation may generate two phytolith pools in soils: fresh, labile phytoliths as a direct source of bioavailable Si, and aged phytoliths preserved from dissolution within soil aggregates (Vander Linden et al., 2021). This view accounts for previous observations (Meunier et al., 2014). It could reconcile an apparent paradox: considering phytoliths as the major reservoir of mobile Si in the soil-to-plant system (Erhart, 1963; Conley, 2002; Meunier, 2003) because of their high dissolution rate (Fraysse et al., 2009), using phytoliths as microfossils to reconstruct paleoenvironments (Strömberg et al., 2018) because of their stability over millennia (Monger and Kelly, 2002).

Soil aggregates are expected to embed fine-sized phytoliths and likely protect them (Li et al., 2020, Vander Linden et al., 2021). However, the mechanisms of intimate interaction between phytolith and other soil constituents are poorly understood. Equally, the role of the aggregation process in controlling Si mobility is unknown. Another major uncertainty lies in the fact that the reservoir of bioavailable Si may be fed by biogenic and mineral sources (White et al., 2012). Here we analyzed the role of aggregation in releasing bioavailable Si from phytoliths entrapped in aggregates of controlled composition. We used synthetic aggregates incubated from mixtures made of purified plant-extracted phytoliths, organic matter (OM), sand-sized quartz, and clay-sized aluminosilicate and Fe oxide in fixed proportions. Amorphous minerals have a higher SSA, and are thus more prone to aggregation than their crystalline counterparts (Harsh et al, 2002; White and Dixon, 2002). In this light, we compared two models, amorphous (*Am*) and crystalline (*Cryst*), differing only in the amorphous and crystalline nature of the clay mineral and Fe oxide, with the other components held constant. We further quantified the

release of bioavailable Si as impacted by aggregation, and traced its source using Si/Al and Ge/Si atomic ratios.

Materials and methods

Individual components. *Phytoliths* were extracted from rice plants as described by Li et al. (2019). Rice seeds (*Oryza sativa indica* IR64; IRRI) were germinated on a polystyrene plate floating on a Yoshida nutrient solution (Yoshida, 1981) in 5 plastic tanks of 25 L. The seeds were placed in holes perforating the plate. The nutrient solution was then enriched with H_4SiO_4 at a concentration of 40 mg l^{-1} (Henriet et al., 2006). At grain harvesting stage, rice leaves were collected, washed successively with deionized water, HCl 1 M, 70% ethanol, rinsed with deionized water (Kelly, 1990) and grinded. They were then digested at 120°C in a concentrated HNO_3/H_2O_2 (70/30%) mixture for about 10 days until complete mineralization of OM. Finally, they were isolated after filtration at 0.2µm (Cornelis et al., 2010a). The phytolith particles were washed using deionized water through wash-centrifugation-filtration cycles (13,100 rpm, 5 min) till constant pH and electrical conductivity equal to that of deionized water. They were oven-dried at 50 ºC for 2 days. *Quartz* was supplied by Merck KGaA Co, Darmstadt, Germany, the particles being of calibrated size 330-500 µm. *Organic matter* (OM) was oven-dried and finely ground Egyptian clover (*Trifolium alexandrinum*), rich in nitrogen (N) with a C/N ratio of 24.3. This low C/N ratio favored OM decomposition, thus providing fine-sized organic substances involved in associations with clay-sized minerals in microaggregates (Totsche et al., 2018). *Kaolinite* was collected in the *Charentes* basin, in early Eocene (Sparnacian-Cuisan) siderolithic sandy-clay deposits derived from lateritic alteration of French Massif Central granites (Yvon et al., 1982). The kaolinite contained minor amounts of Fe ($Si_2Al_{2-x}Fe_xO_5(OH)_4$), $x \leq 0.02$) (Mestdagh et al. 1982), with SSA ranging from 9 to 75 $m^2\ g^{-1}$ and Si/Al = 1.01 (Cases et al. 1982; Delineau et al. 1994). Its cation exchange capacity (CEC) was between 5 and 12 $cmol_{(+)}\ kg^{-1}$, most of the exchange sites being due to amphoteric dissociations on edge faces (Cases et al., 2000). *Allophane* was synthesized following Ohashi et al. (2002). Briefly, 0.1 M Na_4SiO_4 and $AlCl_3$ solutions were mixed, stirred at room temperature for 1 h, and stored in an oven at 95 °C for 90 h. The clear supernatant was decanted. The precipitate was washed with deionized water by successive dispersion/centrifugation (3000 RPM for 10 min) cycles to remove

NaCl until negative $AgNO_3$ test, and eventually freeze-dried. *Iron oxides* were synthesized according to Cornell and Schwertmann (1996). For *ferrihydrite*, a freshly prepared 0.1M $Fe(NO_3)_3$ solution (250 ml) was slowly neutralized by 1M NaOH (70 ml), brought dropwise to pH 7.5. The red/brown precipitate was separated by centrifugation (3500 rpm, 10 min). It was dialyzed (dialysis-membrane SPECTRA/POR 4, MWCO = 12-14000, Ø = 29 mm) against deionized water until electrical conductivity was stable at 1-2 μS for 4 h. The dialyzed product was freeze-dried. For *goethite*, a freshly prepared 1 M $Fe(NO_3)_3$ (100 ml) solution was neutralized by 5M NaOH (70 ml) under intense stirring and brought to pH > 12. The red/brown precipitate was dried in the mother liquid at 70 °C for 60 h, and turned to yellow/brown. The precipitate was washed with deionized water through washing-centrifugation cycles (13,100 rpm, 15 min) until pH and electrical conductivity were stable, respectively, at 5.5 and 1-2 μS cm^{-1}. The precipitate was oven-dried at 50 °C for 48 h.

Mixtures and aggregates. *Bulk mixtures* were composed of (g kg^{-1}): OM (50), aluminosilicate mineral (370), iron (Fe) oxide (60), quartz (500) and rice phytolith (20). Two models, amorphous (*Am*) and crystalline (*Cryst*), were defined. They differed only by the constitution of the couple aluminosilicate–Fe oxide, which was allophane–ferrihydrite and kaolinite–goethite in the *Am* and *Cryst* model, respectively. All other components (OM, quartz, phytolith) remained in identical proportions. These assemblages simulate pedological contexts of variable-charge soils. For the amorphous (*Am*) model, they compare to allophane-rich Andosols (Aomine and Jackson, 1959; Arnalds, 2004; Kaufhold et al., 2010; Parfitt, 2009; Russel et al., 1981). For the crystalline (*Cryst*) model, they compare to ferrallitic soils such as can occur in intertropical regions (Ahn, 1970; Sanchez, 2019, Van Wambeke, 1992). For each model, the bulk mixtures were divided into two parts, designed as *mixtures* and *aggregates*, both in triplicate. The *mixtures* were in fact the initial bulk mixtures, just juxtaposing the individual components, not subjected to watering and ageing. The *aggregates* were produced from bulk mixtures that were irrigated with deionized water using a liquid/solid ratio 0.6/1.0 g g^{-1}, incubated in darkness at 20 °C for 32 days, and freeze-dried (Filimonova et al., 2016). They were then gently grinded and sieved at 2 mm.

Characterization of phytoliths and mineral constituents. *X-ray diffraction* (XRD, Bruker D8 Advance diffractometer) analysis was performed on randomly oriented powder samples without any treatment using Cu*K*α radiation (I = 0.15418 nm, 40 kV, 30 mA, 2θ = 1°/min). *Microscopy*. Scanning electron microscopy was performed without any chemical pretreatment using a field emission gun SEM (FEG-SEM; Zeiss Ultra55). *Surface properties*. N_2 sorption-desorption isotherms were performed at 77 K (-196 °C) using Micromeritics ASAP2020 analyzer. Before analysis, all samples (0.2 g) were degassed for 2 h at 200 °C under dynamic vacuum (10^{-3} mbar). We looked for a compromise between complete water removal and mineral transformation. Thus, we also carried out a 24 h degassing (10^{-3} mbar) for goethite, ferrihydrite and allophane at 100 °C, and for ferrihydrite and allophane at 40 °C to avoid micropores collapse (Maeda and Warkentin, 1975). The BET equation (Brunauer et al., 1938) was applied to N_2 sorption/desorption data to derive SSA. Zeta potential (ζ) was determined with a ζ analyzer (Zetasizer ULTRA/Pro, Malvern, UK), using suspensions (solid/liquid ratio 10 mg/10ml), in which electrical conductivity and pH were measured. *Elemental analysis*. Total concentrations of Si, Al, Fe were measured in triplicate on phytoliths, mineral constituents and OM. They were determined by Inductively Coupled Plasma - Atomic Emission Spectrometry (ICP–AES, Jarrell Ash Iris Advantage) after calcination at 500°C for 24h, fusion in Li-metaborate + Li-tetraborate at 1000 °C (Chao and Sanzolone, 1992), and then ash dissolution with a diluted 10% HNO_3 solution. Germanium (Ge) concentration was measured by ICP Mass Spectrometry (ICP-MS) in powder samples (100 mg) after alkaline fusion using sodium peroxide (Na_2O_2) in a glassy carbon crucible, heating to 600–800 °C until complete reaction, and dissolution of the residual vitreous mass with a diluted 2% HNO_3 solution (500ml). Accuracy and long-term repeatability of Ge analysis were well assessed. The detection limit was 0.8×10^{-3} ppb. The analytical measurement precision was ± 2%. The BHVO-2 standard (basalt rock powder) was systematically dosed every two samples in each analytical series. The C and N concentrations of OM were measured by a Flash 2000 Elemental Analyzer (Thermo Fisher Scientific, Waltham, MA, USA). *Selective extractions*. The contents of dark oxalate-extractable (o) Si, Al and Fe, and sodium (Na) dithionite-citrate-bicarbonate (DCB) extractable (d) Fe were determined in triplicate in the respective extracts by inductively coupled plasma - atomic emission spectrometry (ICP–AES) following Dahlgren (1994). Oxalate extraction was carried out in darkness by shaking for 4 hours 1 g

sample in 100 ml ammonium oxalate - oxalic acid buffer 0.2M pH3 at 20 °C. The extraction of Fe_d was done at 80°C for 0.75 g sample in 30 ml 0.3M Na citrate + 3.75 ml 1M Na bicarbonate + 3 x 0.75g Na dithionite under agitation for 15 minutes.

Characterization of aggregates. Aggregates were visualized by SEM as described above on samples sieved at 2mm, and by Transmission Electron Microscopy (TEM) on samples sieved at 250 μm, using a LEO 922 Omega Energy Filter Transmission Electron Microscope operating at 120 kV.

Specific extractions from individual components, mixtures and aggregates. The Na_2CO_3- and $CaCl_2$-extractable Si and Al concentrations were determined through kinetic extractions in triplicate to assess the contents of biogenic silica (DeMaster, 1981; Koning et al., 2002; Saccone et al., 2006) and bioavailable Si (Haysom and Chapman, 1975; Sauer et al., 2006), respectively. *Na_2CO_3 extraction*. Thirty mg of sample was mixed in 40ml of Na_2CO_3 0.1M, pH = 11.2, and digested for 5 h at 85 °C. One ml of extraction solution was collected at 1, 2, 3, 4 and 5 h, then neutralized and acidified by adding 100 μl of 7M HNO_3 to analyze dissolved Si and Al using ICP–AES. The extracted Si and Al (Na_2CO_3-Si and -Al) were plotted against time. Corrections were made for the simultaneous alkaline dissolution of amorphous and crystalline Si using time course extractions (DeMaster, 1981; Koning et al., 2002). We assumed that (i) most of the amorphous pool dissolved within the first 2 h of extraction, and (ii) the clay minerals released Si at a much slower and constant rate during the whole extraction. The concentration of amorphous Si (ASi) was determined by the intercept of the linear part of the plot, using the lm function of the R programming language to fit a first-order kinetic model (Cornelis et al., 2011). This procedure was applied to estimate amorphous Al (AAl). *$CaCl_2$ extraction*. We carried out a kinetic extraction (Li et al., 2019) using a solid:liquid ratio 2g:20ml (0.01M $CaCl_2$) in a plastic centrifuge tube through continuously shaking under darkness at 20 °C. The 2:20 solid:liquid ratio was kept constant using replicates for both the extraction and analysis. At each time step (6, 12 and 24 h; 2, 4, 8, 16, 32 and 64 days), the collected suspension (20 ml) was centrifuged at 3,000g for 20 min. The supernatant (15ml) was filtered and separated in two aliquots to measure pH (5 ml) and solutes concentrations (10ml), respectively. In its turn, the latter extract was separated in two aliquots of 5 ml to determine, as described above, Si and Al concentration by ICP-AES at each kinetic step, and Ge concentration at 16h and 64d by IC-MS, respectively. Each 5-ml aliquot was diluted with Milli-Q water by 10 times before

assaying Si and Al, but by 2.5 times before dosing Ge. In both cases, each 5 ml aliquot was acidified by adding 50 µl 7M HNO_3. These determinations were aimed to quantify the release of bioavailable Si as well as to trace its origin using the Si/Al and Ge/Si ratios. Following Houba et al. (2000), and Jones and Willett (2006), we measured dissolved OC (DOC) in the 0.01M $CaCl_2$ extract at 16h with a TOC analyzer (TOC-L, CPN; Shimadzu).

Results

Basic characteristics of the materials. The individual components exhibited typical shapes and morphologies as visualized in Fig. S1. The XRD data showed in Fig. 1: (a) broad reflections at 0.34 and 0.22 nm typical for allophane (Harsh et al, 2002; Ohashi et al., 2002); (b-c) features consistent with those for 2-line ferrihydrite and goethite (Bigham et al., 2002; Cornell and Schwertmann, 1996; Delstanche et al., 2009; Jambor and Dutrizac, 1998); (d) diffraction band at 5.5–3.2 nm centered at ~4.3 nm characteristic for rice phytolith (Trinh et al., 2017; Nguyen et al., 2021); (e) intense reflections at 0.715 nm (d_{001}) and 0.356 nm (d_{002}) of kaolinite (White and Dixon, 2002) and (f) at 0.334 and 0.426 nm for quartz (Monger and Kelly, 2002). Elemental analyses (Table 1) showed expected values of the Si/Al ratio for allophane (0.72) and kaolinite (0.99). The oxalate and DCB extraction data (Table S1) confirmed the amorphous character of allophane and ferrihydrite, and the crystalline nature of kaolinite and goethite. The Fe_o/Fe_d ratio was 0.004 for goethite, certifying its crystalline form, and 0.86 for ferrihydrite, attesting its amorphous nature (Cornell and Schwertmann, 1996). The Ge/Si ratio decreased in the order (µmol mol^{-1}): kaolinite (4.37) > quartz (2.10) > allophane (0.94) > phytolith (0.41) (Table 1).

Surface properties of components. The SSA values (Table 2) decreased in the sequence (m^2 g^{-1}): allophane (306–231) > ferrihydrite (264–242) > phytolith (190) > goethite (132–35) > kaolinite (24) > quartz (1). The degassing temperature had little effect on ferrihydrite SSA (242–264 m^2 g^{-1}), but a large one on the SSA of goethite (132–35 m^2 g^{-1}) and allophane (306–231 m^2 g^{-1}). The values of zeta potential (ζ) (Table 2) were negative for phytolith, kaolinite and quartz, and positive for allophane, ferrihydrite and goethite. Given that (i) ζ varies with pH and (ii) ionic strength does not impact the pH of the

isoelectric point (pH_{IEP}) at which $\zeta = 0$, we could use literature data, as shown in Fig.2, to plot ζ against pH for the selected components. This graph shows that pH_{IEP} at ~9.6 (goethite), ~8.0 (ferrihydrite), ~5.6 (allophane), ~3.6 (kaolinite) and ~2.6 (phytolith).

Aggregates properties. The SEM images showed phytolith particles embedded in aggregate matrix (Fig. 2a-b) while TEM micrographs illustrated intimate associations of fine–sized aluminosilicate and Fe oxide (Fig. 2c-d). At identical OC concentration in mixtures and aggregates, DOC release was lower in the *Am* model than in the *Cryst* one (Fig. 2e-f), as well as in the aggregate relatively to the unaggregated mixture.

Na_2CO_3 extractable Si and Al. The Na_2CO_3 extraction kinetics traced the time-evolution of Si (Na_2CO_3-Si) and Al (Na_2CO_3-Al) for the individual components (Fig. S3), mixtures and aggregates (Fig. S4). Aluminum was not detected in phytoliths, while Na_2CO_3-Si and -Al were not detected in quartz and OM (Table 3). The kinetic data were used to estimate amorphous Si (ASi) content (Fig. 3, Table 3), which decreased in the order (g kg^{-1}): phytolith (272) > allophane (44) > kaolinite (1.2), and *Am* mixture (22.4) > *Am* aggregate (15.3) > *Cryst* mixture (9.0) > *Cryst* aggregate (6.3), with lower ASi contents in aggregates than in mixtures. Using the same technique (DeMaster, 1981) to estimate amorphous Al (AAl), the Si/Al ratio (Table 2) was 0.5 for allophane, 1.1 for kaolinite, 0.76 for *Am* mixture, 1.1 for *Am* aggregate, 11 for *Cryst* mixture, 54 for *Cryst* aggregate.

$CaCl_2$ extractable Si, Al and Ge. As shown in Fig. 4, $CaCl_2$-Si released at pH 3.8-4.0 (Fig. 4e) decreased in the order (g kg^{-1}, 16h-64d): allophane (7.9-29) > phytolith (0.2-5.6) > kaolinite (0.01-0.15) (Fig. 4a-c), and was negligible for quartz (10^{-3}-0.02) (Fig. 4d, Table 4). $CaCl_2$-Si and -Al were not detected for OM. The release rate of Si in $CaCl_2$ ($RR\text{-}Si_{CaCl2}$) was 9-12 and 40-52 times higher for allophane than for phytolith and kaolinite, respectively (Fig. 4f), and negligible for quartz. The Si/Al ratio increased during the 64d extraction from 0.8 to 1.2 and 0.9 to 7.2 for allophane and kaolinite, respectively (Table 4, Fig. S5). Fig. 5 showed that $CaCl_2$-Si was larger in *Am* mixtures and aggregates than in their *Cryst* counterparts. Indeed, $CaCl_2$-Si decreased in the order (16h–64d, g kg^{-1}): *Am* mixture (0.33–3.72) > *Am* aggregate (0.27–0.95) > *Cryst* mixture (0.06–0.48) ≥ *Cryst* aggregate (0.1–0.39). Thus, $CaCl_2$-Si at 64d was nearly 8 times greater in the *Am* mixture (3.72 g kg^{-1}) than in the *Cryst*

mixture (0.48 g kg^{-1}). It was reduced after aggregation by 4 in the *Am* model, and only but significantly by 1.2 in the *Cryst* model (Fig. 5 Table 4). In the *Cryst* model, $CaCl_2$-Al was negligible relatively to $CaCl_2$-Si, resulting in huge Si/Al ratio, above 800 at 64d (Fig. 5h, Table 4). In contrast, in the *Am* model, both Si and Al were extracted by $CaCl_2$ in substantial amounts (Fig. 5a, e, Table 4), resulting in Si/Al ranging from 0.6 to 0.98 in the *Am* mixture, and from 0.74 to 0.43 in the *Am* aggregate (Fig. 5g). As shown in Fig. 6, the pH values of the $CaCl_2$ extract (pH_{CaCl2}) sharply differed between models. They ranged from 3.8 to 4.9 in the *Am* model and between 5.0 and 7.8 in the *Cryst* model, unlike for phytolith, allophane and kaolinite ($pH \leq 4$) (Table 4). The $CaCl_2$ extractable Si and Ge concentrations measured at 16h and 64d (Table 4a-d) were used to calculate the Ge/Si molar ratio (μmol mol^{-1}). This ratio significantly differed between components (16h-64d): phytolith (3.15-0.27), allophane (1.31-0.66), kaolinite (24.74-1.83) (Table 4a-b). Equally, Ge/Si significantly differed between mixtures and aggregates (16h-64d): *Am* mixture (0.40-0.21), *Am* aggregate (0.64-0.77), *Cryst* mixture (6.37-1.28), *Cryst* aggregate (1.05-0.5) (Table 4c-d). The variations in Ge/Si are illustrated in Fig.8.

Discussion

Constituents and properties. The nature of individual components was confirmed by XRD, SEM, elemental analysis and selective extraction data (Fig. 1, Fig. S1, Table 1, Table S1). From Table 1, allophane Ge/Si (0.9 μmol mol^{-1}) depended on the Ge content of the Na_4SiO_4 source, and on its fractionation during synthesis (Kurtz et al., 2002). The Ge/Si ratio (μmol mol^{-1}) of the *Charentes* kaolinite (4.3) was close to that of kaolinites in highly weathered soils derived from granite (5.9, Kurtz et al., 2002; 4.8-6.1, Lugolobi et al, 2010), in agreement with their similar ferrallitic origins (Yvon et al., 1982). These values were similar to Ge/Si (μmol mol^{-1}) of kaolinite/halloysite assemblages in strongly weathered B horizons derived from andesitic basalt (4.3-6.4, Opfergelt et al., 2010). Yet, they were below those of kaolinites derived from basalt (~6-12, Kurtz et al., 2002; ~7-14, Qi et al., 2019). The phytolith Ge/Si ratio (0.41 μmol mol^{-1}) was in the range of most available Ge/Si values (0.003-0.5) (Blecker et al., 2007; Cornelis et al, 2010b; Delvigne et al., 2009; Derry et al., 2005; Kurtz and Derry, 2004; Lugolobi et al, 2010; Meek et al., 2016; Seyfferth et al., 2013; White et al., 2012). From the

respective Si and Ge concentrations in allophane, kaolinite, phytolith and quartz, Ge/Si (μmol mol^{-1}) was computed for the *Am* (1.87) and *Cryst* model (2.62), in very good agreement with measured Ge/Si values of *Am* (1.87) and *Cryst* (2.58) mixtures (Table 1). The surface and charge properties of the components were as expected (Sposito, 2016). The impact of the degassing temperature on SSA (Table 2) showed that a compromise had to be reached between water removal, pore collapse and mineral transformation. Upon heating, surface and bulk decomposition reactions of goethite initiated at 200 °C (Ford and Bertsch, 1999), while dehydration of both goethite and ferrihydrite could affect their SSA (Houben and Kaufhold, 2011). For allophane, pore collapse (Maeda and Warkentin, 1975), dehydration and dehydroxylation may occur continually without any clear boundaries (Du et al., 2018), making crucial the compromise described above (Chen et al., 2014). In all cases, allophane and ferrihydrite had a higher SSA than kaolinite and goethite, respectively, thus enhancing aggregation in the *Am* model (Deng and Dixon, 2002). The SSA value of rice phytolith (190 m^2 g^{-1}) was within the range reported for other phytoliths (93-316 m^2 g^{-1}) (Fraysse et al., 2009), but was 5 times higher than those measured for rice phytoliths after heating at 300-400 °C (36-38 m^2 g^{-1}: Nguyen et al., 2021; Trinh et al., 2017). As illustrated in Fig. S2, goethite and ferrihydrite stood out clearly from the other materials with $pH_{IEP} \geq 8$, and thus carried a positive surface charge at pH < 8, whereas allophane, kaolinite and phytolith had pH_{IEP} at ~5.6, ~3.6 and ~2.6, respectively. Such discrepancies, combined with pH_{IEP} of OM generally at ~2–3 (Tombácz and Meleg, 1990), enhanced colloidal interactions and aggregation, particularly in the *Am* model (Deng and Dixon, 2002; Johnston and Tombácz, 2002), as illustrated in the following section.

Aggregation reduced DOC release, and preserved amorphous silicates. Aggregates readily formed after a 32-day incubation (Fig. 2a-b). The SEM images showed phytoliths embedded in aggregates in which OM, clay-sized aluminosilicate and Fe oxides underwent intimate associations (Deng and Dixon, 2002) as revealed by TEM (Fig. 2c-d). As inferred from Fig. S2, attraction of oppositely charged crystal faces of kaolinite and goethite caused flocculation and aggregation (Arias et al., 1995; El-Swaify and Emerson, 1975; Schofield and Samson, 1954; Sposito, 2016; West et al., 2004). Besides electrostatic attraction, kaolinite and goethite interact by anion ligand exchange, surface coordination, and hydrogen

bonds (Wei et al., 2012). These processes enhanced the formation of aggregates able to embed quartz particles (Pinheiro-Dick and Schwertmann, 1996) and stabilize OM (Kretzschmar et al., 1993; Tombácz et al., 2004). Permanent charge soils have an aggregate hierarchy with OM as the main binding agent (Six et al., 2000). In contrast, soils with crystalline variable charge minerals do not show an aggregate hierarchy, but they have Fe and Al oxides as binding agents (Six et al., 2000). These soils have a higher potential to form stable aggregates at low OC concentrations (Denef et al., 2002). In contrast, Andosols with amorphous variable-charged minerals exhibit aggregate hierarchy in which clay-sized composites made of allophane, ferrihydrite and OM bound to them are the main binding agents (Asano and Wagai, 2014). The presence of the composites induces strong aggregation in natural environments (Bartoli et al., 2007; Baumgarten et al., 2013; Churchman and Tate, 1987; Latrille et al., 2003; Parfitt et al., 1988; Warkentin and Maeda, 1980), as well as under laboratory conditions after a 20-day incubation (Filimonova et al., 2016). Here, at identical OC content in mixtures and aggregates, the 32-day aggregation sharply decreased DOC release (Fig. 2e-f) in both models, but DOC release was much lower in the *Am versus* the *Cryst* model. In the latter, a low critical threshold of OC to form aggregates (Denef et al., 2002) likely resulted in a higher DOC release. In the *Am* model, the protective effect on OC was enhanced by aggregation built up from clay-sized composites of allophane, ferrihydrite and OM (Asano and Wagai, 2014; Filimonova et al., 2016; Warkentin and Maeda, 1980), but also likely by OM adsorption on mineral surfaces, and organo-mineral associations (Basile-Doelsch et al., 2015; Chen et al., 2014; Deng and Dixon, 2002; Eusterhues et al., 2005, 2014; Kaiser and Guggenberger, 2007; Kleber et al., 2005, 2015; Lehmann and Kleber, 2015). In any case, measuring DOC release was considered here as a test confirming the aggregation process in both models, the *Am* model enhancing this process even more.

The ASi content estimating biogenic silica (DeMaster, 1981) also differed between the two models and, within each model, between mixtures and aggregates (Fig. 3b). From the respective ASi levels in phytolith, allophane and kaolinite (Table 2), ASi content was computed for the *Am* (22 g kg^{-1}) and *Cryst* model (6 g kg^{-1}), in good agreement with the ranges of ASi values measured in *Am* (22.4–15.3 g kg^{-1}) and *Cryst* (9–6.3 g kg^{-1}) mixtures and aggregates (Table 2, Fig. 3b). The decrease in ASi induced by aggregation was, however, larger in the *Am* than in the *Cryst* model, suggesting a larger ASi

preservation in the former because of a stronger aggregation due to the factors discussed above (Asano and Wagai, 2014; Filimonova et al., 2016). Despite the short ageing period (32d), our experimental data were in agreement with previous studies (Li et al., 2020b; Vander Linden et al., 2021) suggesting the coexistence of free and labile phytoliths with phytoliths preserved in soil aggregates. Yet, considering the total phytolith Si content (381 g kg^{-1}, Table 1), ASi (272 g kg^{-1}, Table 3) underestimated the phytolith pool. Moreover, it did not exclusively reflect it since the Si/Al ratio of the ASi compounds was as low as 0.76-1.05 in the *Am* model (Table 3), revealing allophane dissolution in Na_2CO_3. In contrast, kaolinite dissolution (1.16 g kg^{-1}, Table 3) was negligible in the *Cryst* model, with Si/Al ratio of the ASi compounds equal to 11.4 and 54.6 in the *Cryst* mixture and aggregate, respectively (Table 3). Thus, allophane and phytolith were the major, if only, ASi components in the *Am* and *Cryst* model, respectively. This observation raised concerns about the relevance of the technique (DeMaster, 1981) for targeting the phytolith pool in soil, as previously questioned (Li et al., 2019; Li et al., 2020b; Meunier et al., 2014; Vander Linden et al., 2021).

Release of bioavailable Si is impacted by aggregation, constituents and pH. Considered to target bioavailable Si (Haysom and Chapman, 1975; Sauer et al., 2006), the $CaCl_2$-extractable Si concentration ($CaCl_2$-Si) is usually determined in one extract after stirring for 16 h (Haysom and Chapman 1975; Sauer et al., 2006), 5 h (Henriet et al., 2008; Houben et al., 2014) or 1 h (Korndörfer et al., 1999). Here, we followed the kinetics of Si release (Li et al., 2019) and attempted to relate $CaCl_2$-Si to specific Si-bearing phases. Our data (Fig. 4, Fig. 5, Table 4) highlighted the following: (i) the *Am* model had a higher efficiency to form aggregates preserving Si-releasing constituents, (ii) the nature of these constituents (a.o. SSA, surface charge), and/or (iii) pH were also operationally involved in Si release. As discussed above, the higher efficiency of the *Am* model to form aggregates, preserve OC and ASi, and reduce Si release, was due to the specific surface charge properties of allophane and ferrihydrite compared to kaolinite and goethite. Of particular impact were their high SSA and surface charge (Harsh et al, 2002; Hiemstra, 2018; Hiemstra et al., 2007; White and Dixon, 2002), and the implication of clay-sized composites of allophane, ferrihydrite and OM as main binding agents (Asano and Wagai, 2014; Filimonova et al., 2016). In both *Am* and *Cryst* models, the protective effect of Si-releasing components on Si release was enhanced by aggregation, but possibly also by H_4SiO_4

adsorption onto oxide surfaces (Delstanche et al., 2009; Hiemstra, 2018; Hiemstra et al., 2007; Jones and Handreck, 1963). Since $CaCl_2$-Si release from quartz was negligible, and not detected for OM, the only sources of bioavailable Si were phytolith, along with allophane and kaolinite in the *Am* and *Cryst* mixtures and aggregates, respectively (Fig. 4, Table 4). The Ge/Si ratio was used to trace silica sources in rivers (Conley, 2002, Derry et al., 2005; Frings et al., 2021; Murnane and Stallard, 1990) and soil solutions (Cornelis et al., 2010b). Here, we combined both the Si/Al and Ge/Si ratios to identify the components releasing Si in $CaCl_2$. Aluminosilicate dissolution is induced by protonation and/or by ligands that form complexes with metals (Sposito, 2016). In the absence of pH buffering, using 0.01M $CaCl_2$ decreases the pH of the extracting solution (pH_{CaCl2}) due to exchange of H^+ by Ca^{2+} ions on negatively charged surface sites. The dissolution rates observed here at $pH \leq 4$ for allophane and kaolinite (Fig. 4a, b, e; Table 4) corroborated previous studies. Allophane indeed rapidly dissolves in acid conditions (Pačes, 1978; Dobrzyński, 2006; Wang et al., 2020), and is metastable to kaolinite and halloysite (Su and Harsh, 1998, Dobrzyński, 2006). Its dissolution is enhanced by Al-complexing anions (Su and Harsh, 1993; Harsh et al., 2002). Allophane dissolves rapidly in dilute solutions, with dissolution rates one order of magnitude higher than crystalline phases of similar composition (Ralston, 2021), confirming previous observations for both synthetic and natural allophanes (Harsh et al, 2002; Henmi et al, 1999). Allophane dissolution is greater with low Si/Al ratios (Henmi et al., 2001; Su and Harsh, 1998), with Al-rich allophanes being even less stable than imogolite (Harsh et al., 2002; Su and Harsh, 1998; Dobrzyński, 2006). Here, the dissolution of Al-rich allophane (Si/Al = 0.72) was non-stoichiometric with $CaCl_2$-Si/Al ratio increasing from 0.82 to 1.2 (Table 4, Fig. S5c). Despite an initial preferential leaching of Al (Henmi et al., 1999; Ralston et al., 2021; Wang et al., 2020), the progressive increase in Si/Al ratio with increasing time indicated that Al could be reprecipitated or re-adsorbed (Ralston et al., 2021). The first increase and then decrease in $CaCl_2$-Ge/Si ratio (Table 4) could be attributed to Ge partitioning during the dissolution-precipitation process (Kurtz et al., 2002). The dissolution of kaolinite (Si/Al = 0.99) at $pH \leq 4$ (Fig. 4b, e) was weaker and slower than that of allophane (Fig. 4f), and was non-stoichiometric since $CaCl_2$-Si/Al ratio increased from 0.96 to 7.2 (Table 4). Acidic conditions and low silica activity enhanced kaolinite dissolution (Karathanasis, 2002), starting with preferential removal of Al (Carroll-Webb and Walther, 1988; Huertas et al., 1999; Xie and

Walther, 1992), which can be re-adsorbed (Wieland and Stumm, 1992; Yang and Steefel, 2008). The variation of $CaCl_2$-Ge/Si ratio (24.7-1.8 μmol mol^{-1}, Table 4) was consistent with the model for Ge-Si equilibrium fractionation in kaolinite (Perez-Fodich and Derry, 2020), i.e., an abrupt increase in the aqueous Ge/Si ratio (1.2 μmol mol^{-1}) induced by mineral breakdown followed by its rapid decrease (0.4 μmol mol^{-1}). Unlike for allophane and kaolinite, phytolith dissolution begins with Si removal (Dove, 1994), i.e., the breaking of the Si–O bond that is more covalent than typical metal-oxygen bonds (Sposito, 2016). It is driven by silica undersaturation, enhanced by the 'salt effect' in dilute solutions and the increase in net negative charge (Dove, 1994; Dove et al., 2005; Dove et al., 2008), and thus by pH increase (Fraysse et al., 2009). Here, phytolith dissolution at pH ~3.6 (Fig. 4c, e, Table 4) was weaker and slower than that of allophane, but stronger and quicker than that of kaolinite (Fig. 4f), while the variation of the $CaCl_2$-Ge/Si ratio (3.15-0.27 μmol mol^{-1}) was due to Ge fractionation during dissolution (Blecker et al., 2007; White et al., 2012). The dissolution rates of allophane, phytolith and kaolinite were compared in Table 5 to literature data obtained in similar acidic conditions. Worth noting was the relatively high dissolution rate of allophane, confirming that amorphous aluminosilicate was a substantial source of bioavailable Si as previously suggested (Vandevenne et al., 2015; White et al., 2012; Cornu et al., 2022). Thus, the values of $CaCl_2$-Si, Si/Al and Ge/Si ratios in the $CaCl_2$ extracts (Table 4, Fig. 7) confirmed that the main sources of bioavailable Si were phytolith and allophane in the *Cryst* and *Am* and model, respectively. Plotting our experimental data (Table S2) in the Al_2O_3–SiO_2–H_2O stability diagram (Fig. 8) further illustrated that H_4SiO_4 activity was controlled by phytolith in the *Cryst* mixture, and by allophane in the *Am* mixture. Yet, in the *Am* aggregates, both phytolith and allophane ruled silica activity (Fig. 8), but the Si/Al ratio of the $CaCl_2$ extracts showed that allophane was the largely dominant contributor of dissolved Si. In addition, pH exerted a crucial role in phytolith dissolution in the *Cryst* model (Fig. 6). The release of bioavailable Si was thus impacted by aggregation, the nature of constituents and pH. In the *Am* model, acidic conditions enhanced allophane breakdown whereas phytolith dissolution occurred in the *Cryst* model, due to higher pH and kaolinite stability. Furthermore, our data pointed an interesting convergence in that aggregation reduced ASi content as well as the release of DOC and bioavailable Si. Our data were indeed in line with the literature data

reported in Fig. 9, showing that the *Am* aggregate stood out from other soil materials, but was quite comparable to the highly aggregated *Chernozem*, also known to store OC.

Implications and conclusion

From a geochemical perspective, our study shows how the combined effect of aggregation, the nature of constituents and pH has an impact on the release of bioavailable Si in soil materials. The findings provide insight for a better understanding of the processes that explain the origin of DSi and the resilience of phytoliths over millennia in soils and sediments. They also decipher the role of clay minerals, amorphous and crystalline, upon Si mobility and transfer to rivers and oceans. Also, our results have methodological implications.

Phytoliths are renowned to contribute massively to the continental export of dissolved silica towards rivers and oceans (Conley, 2002; Derry et al., 2005) due to their relatively high dissolution rate, which is 10^2-10^4 higher than that of crystalline clay minerals at common pH values of soil solution (4-8) (Fraysse et al., 2009). Here we show that phytoliths can be removed from the silica cycle by aggregation of particles in soils and sediments, a process that can generate two pools: fresh, labile *versus* aged, entrapped phytoliths (Li et al., 2020b; Meunier et al., 2014; Vander Linden et al., 2021). Aggregation can thus be one of the processes that preserves phytoliths by entrapping them in soils and sediments, enabling their use as paleo-indicators (Cabanes et al., 2012; Cabanes et al., 2015; Laugier et al., 2022). Other processes such as phytolith coating by Al and/or Fe oxide might contribute to their preservation (Strömberg et al., 2018). Specific features of phytoliths also impact their resilience, e.g., morphotype (Cabanes et al, 2012), surface roughness and its evolution (Puppe and Leue, 2018).

We further show that the pool of amorphous aluminosilicates is a substantial source of bioavailable Si, as presumed earlier (Clymans et al., 2011; Vandevenne et al., 2015; White et al., 2012; Cornu et al., 2022). This is due to their metastable character (Dobrzyński, 2006; Pačes, 1978; Su and Harsh, 1998) and rapid dissolution (Harsh et al., 2002, Ralston et al., 2021), particularly in acidic conditions (Wang et al., 2020) wherein their dissolution rate can even be higher than that of phytolith. More generally, crystalline clay minerals such as fine-sized smectite and to a lesser extent kaolinite may also dissolve and release Si depending on pH conditions and silica activity, land use and soil management (Caubet

et al., 2020; Irfan et al., 2017; Keller et al., 2021). Actually, significant clay mineralogy changes occur on short time scales (Cornu et al., 2012), smectite being a privileged reactive proton consumer (Brahy et al., 2000). In this respect, smectite dissolution in soil may significantly contribute to the export of dissolved silica (Violette et al., 2010) and, presumably, to the pool of bioavailable Si as measured in $CaCl_2$ (Jouquet et al., 2020). Clay minerals significantly contribute to soil aggregation because of their surface and charge properties (Deng and Dixon, 2002; Johnston and Tombácz, 2002; Sposito, 2016). Besides, they are generally much more abundant in soils than phytoliths, and can thus be a significant source of dissolved Si, depending on clay content and nature, pH, silica activity, land use and soil management. In this regard, using a combination of tracers such as Si/Al and Ge/Si under known pH conditions, as proposed here, is essential to identify sources releasing Si in low saline solution.

Silicon fluxes to the biosphere and hydrosphere enhance the positive effects of Si on plant vigor and carbon fixation by marine diatoms (Berner, 1997; Conley, 2002; Coskun et al., 2019). The biological cycle of Si is thus critical in primary productivity and C cycling in both terrestrial and marine ecosystems (Conley and Carey, 2015). Therefore, the fate of Si forms in soil is at the core of major challenges facing global change and sustainable agriculture. In this respect, soil clay minerals, in particular poorly crystalline, can exert a pivotal role in supplying aqueous silica, thereby enhancing the sustainability of agricultural ecosystems (Irfan et al., 2017). They thus deserve a specific attention in studies on silica cycle.

Declaration of Competing Interest

All authors contributed to paper writing and revision. The authors declare that there are no conflicts of interest.

Acknowledgements

Z. Li is supported by the *Fonds National de la Recherche Scientifique* (FNRS) of Belgium, as *Chargé de recherches*. This research was supported by FNRS, and *Wallonie-Bruxelles International* (WBI) for supporting the *Partenariats Hubert Currien Tournesol*. The authors warmly thank A. Iserentant, E.

Devos, L. Monin and C. Givron for laboratory assistance in the analytical platform MOCA, UCLouvain, and J.-F. Statsyns for surface analysis at IMCN-MOST, UCLouvain.

Appendix A. Supplementary Material

References

Ahn P. M. (1970) *West African soils*. Oxford University Press, London.

Aomine S. and Jackson M. L. (1959) Allophane determination in Ando soils by cation-exchange capacity delta value. *Soil Sci Soc Am J.* **23**, 210-214.

Arias M., Barral M. T. and Diaz-Fierros F. (1995) Effects of iron and aluminium oxides on the colloidal and surface properties of kaolin. *Clays Clay Miner.* **43**, 406-416.

Arnalds O. (2004) Volcanic soils of Iceland. *Catena* **56**, 3-20.

Asano M. and Wagai R. (2014) Evidence of aggregate hierarchy at micro- to submicron scales in an allophanic Andisol. *Geoderma* **216**, 62-74.

Au P.-I., Clode P., Smart R. S. C. and Leong Y.-K. (2015) Surface chemistry–microstructure–rheology of high and low crystallinity KGa-1b and KGa-2 kaolinite suspensions. *Colloids Surf. A Physicochem. Eng. Asp.* **484**, 354-364.

Bartoli F. (1983) The biogeochemical cycle of silicon in two temperate forest ecosystems. *Ecol. Bull.* **35**, 469-476.

Bartoli F. (1985) Crystallochemistry and surface properties of biogenic opal. *J. Soil Sci.* **36**, 335-350.

Bartoli F., Poulenard A. J. and Schouller B. E. (2007) Influence of allophane and organic matter contents on surface properties of Andosols. *Eur. J. Soil Sci.* **58**, 450-464.

Basile-Doelsch I., Balesdent J. and Rose J. (2015) Are interactions between organic compounds and nanoscale weathering minerals the key drivers of carbon storage in soils? *Environ. Sci. Technol.* **49**, 3997-3998.

Baumgarten W., Dörner J. and Horn R. (2013) Microstructural development in volcanic ash soils from South Chile. *Soil Tillage Res.* **129**, 48-60.

Berner R. A. (1997) The rise of plants and their effect on weathering and atmospheric CO_2. *Science* **276**, 544-546.

Bigham J. M., Fitzpatrick R. W. and Schulze D. G. (2002) Iron oxides. *Soil mineralogy with environmental applications* **7**, pp.323-366.

Blecker S. W., King S. L., Derry L. A., Chadwick O. A., Ippolito J. A. and Kelly E. F. (2007) The ratio of germanium to silicon in plant phytoliths: quantification of biological discrimination under controlled experimental conditions. *Biogeochemistry* **86**, 189-199.

Brahy V., Titeux H. and Delvaux B. (2000) Incipient podzolization and weathering caused by complexation in a forest Cambisol on loess as revealed by a soil solution study. *Eur. J. Soil Sci.* **51**, 475-484.

Brunauer S., Emmett P. H. and Teller E. (1938) Adsorption of gases in multimolecular layers. *J. Am. Chem. Soc.* **60**, 309-319.

Cabanes D. and Shahack-Gross R. (2015) Understanding fossil phytolith preservation: The role of partial dissolution in paleoecology and archaeology. *PLoS One* **10**, e0125532.

Cabanes D., Gadot Y., Cabanes M., Finkelstein I., Weiner S. and Shahack-Gross R. (2012) Human impact around settlement sites: a phytolith and mineralogical study for assessing site boundaries, phytolith preservation, and implications for spatial reconstructions using plant remains. *J. Archaeol. Sci.* **39**, 2697-2705.

Carroll-Webb S. A. and Walther J. V. (1988) A surface complex reaction model for the pH-dependence of corundum and kaolinite dissolution rates. *Geochim. Cosmochim. Acta* **52**, 2609-2623.

Cases J.-M., Liétard O., Yvon J. and Delon J.-F. (1982) Étude des propriétés cristallochimiques, morphologiques, superficielles de kaolinites désordonnées. *Bull. Minéral.* **105**, 439-455.

Cases J.-M., Villiéras F. and Michot L. (2000) Les phénomènes d'adsorption, d'échange ou de rétention à l'interface solide–solution aqueuse. 1. Connaissance des propriétés structurales, texturales et superficielles des solides. *C. R. Acad. Sci., Ser. 2, Earth Planet. Sci.* **331**, 763-773.

Caubet M., Cornu S., Saby N. P. and Meunier J.-D. (2020) Agriculture increases the bioavailability of silicon, a beneficial element for crop, in temperate soils. *Sci. Rep.* **10**, 1-11

Chao T. and Sanzolone R. (1992) Decomposition techniques. *J. Geochem. Explor.* **44**, 65-106.

Chen C., Dynes J. J., Wang J. and Sparks D. L. (2014) Properties of Fe-organic matter associations via coprecipitation versus adsorption. *Environ. Sci. Technol.* **48**, 13751-13759.

Chorover J., Amistadi M. K. and Chadwick O. A. (2004) Surface charge evolution of mineral-organic complexes during pedogenesis in Hawaiian basalt. *Geochim. Cosmochim. Acta* **68**, 4859-4876.

Churchman G. J. and Tate K. R. (1987) Stability of aggregates of different size grades in allophanic soils from volcanic ash in New Zealand. *J. Soil Sci.* **38**, 19-27.

Clymans W., Struyf E., Govers G., Vandevenne F. and Conley D.J. (2011) Anthropogenic impact on amorphous silica pools in temperate soils. *Biogeosciences* **8**, 2281-2293.

Conley D. J. (2002) Terrestrial ecosystems and the global biogeochemical silica cycle. *Glob. Biogeochem. Cycles* **16**, 68-1.

Conley D. J. and Carey J. C. (2015) Silica cycling over geologic time. *Nature Geoscience* **8**, 431-432.

Cornelis J.-T. and Delvaux B. (2016) Soil processes drive the biological silicon feedback loop. *Funct. Ecol.* **30**, 1298-1310.

Cornelis J.-T., Delvaux B., Cardinal D., André L., Ranger J. and Opfergelt S. (2010b) Tracing mechanisms controlling the release of dissolved silicon in forest soil solutions using Si isotopes and Ge/Si ratios. *Geochim. Cosmochim. Acta* **74**, 3913-3924.

Cornelis J.-T., Ranger J., Iserentant A. and Delvaux B. (2010a) Tree species impact the terrestrial cycle of silicon through various uptakes. *Biogeochemistry* **97**, 231-245.

Cornelis J.-T., Titeux H., Ranger J. and Delvaux B. (2011) Identification and distribution of the readily soluble silicon pool in a temperate forest soil below three distinct tree species. *Plant Soil* **342**, 369-378.

Cornell R. M. and Schwertmann U. (1996) The iron oxides: Structures, properties, reactions, occurrences and uses. VCH Verlagsgesellshaft GMBH, Weinheim, Germany, pp.533-555.

Cornu S., Meunier J.-D., Ratie C., Ouedraogo F., Lucas Y., Merdy P., Barboni D., Delvigne C., Borschneck D., Grauby O. and Keller C. (2022) Allophanes, a significant soil pool of silicon for plants. *Geoderma* **412**, 115722.

Cornu S., Montagne D., Hubert F., Barré P. and Caner L. (2012) Evidence of short-term clay evolution in soils under human impact. *C. R. -Geosci.* **344**, 747-757.

Coskun D., Deshmukh R., Sonah H., Menzies J.G., Reynolds O., Ma J.F., Kronzucker H.J. and Bélanger R. R. (2019) The controversies of silicon's role in plant biology. *New Phytol.* **221**, 67-85.

Dahlgren R. A. (1994) Quantification of allophane and imogolite. *Quantitative methods in soil mineralogy*. pp.430-451.

Delineau T., Allard T., Muller J. P., Barres O., Yvon J. and Cases J. M. (1994) FTIR reflectance *vs.* EPR studies of structural iron in kaolinites. *Clays Clay Miner.* **42**, 308-320.

Delstanche S., Opfergelt S., Cardinal D., Elsass F., André L. and Delvaux B. (2009) Silicon isotopic fractionation during adsorption of aqueous monosilicic acid onto iron oxide. *Geochim. Cosmochim. Acta* **73**, 923-934.

Delvigne C., Opfergelt S., Cardinal D., Delvaux B. and André L. (2009) Distinct silicon and germanium pathways in the soil-plant system: Evidence from banana and horsetail. *J. Geophys. Res. Biogeosc.* **114**.

DeMaster D. J. (1981) The supply and accumulation of silica in the marine environment. *Geochim. Cosmochim. Acta* **45**, 1715-1732.

Denef K., Six J., Merckx R. and Paustian K. (2002) Short-term effects of biological and physical forces on aggregate formation in soils with different clay mineralogy. *Plant Soil* **246**, 185-200.

Deng Y. and Dixon J. B. (2002) Soil organic matter and organic-mineral interactions. *Soil mineralogy with environmental applications* **7**, pp.69-107.

Derry L. A., Kurtz C. A., Ziegler K. and Chadwick O. A. (2005) Biological control of terrestrial silica cycling and export fluxes to watersheds. *Nature* **433**, 728-730.

Dobrzyński D. (2006) Silica solubility in groundwater from Permian volcanogenic rocks (the Sudetes Mts., SW Poland) — the role of reversible aluminosilicate solids. *Geol. Q.* **50**, 407-417.

Dove P. M. (1994) The dissolution kinetics of quartz in sodium chloride solutions at 25 degrees to 300 degrees C. *Am. J. Sci.* **294**, 665-712.

Dove P. M., Han N. and De Yoreo J. J. (2005) Mechanisms of classical crystal growth theory explain quartz and silicate dissolution behavior. *PNAS* **102**, 15357-15362.

Dove P. M., Han N., Wallace A. F. and De Yoreo J. J. (2008) Kinetics of amorphous silica dissolution and the paradox of the silica polymorphs. *PNAS* **105**, 9903-9908.

Du P., Yuan P., Liu D., Wang S., Song H. and Guo H. (2018) Calcination-induced changes in structure, morphology, and porosity of allophane. *Appl. Clay Sci.* **158**, 211-218.

Ehrenberg C.G. (1846) Über die Vulkanischen Phytolitharien der Insel Ascension. *Monatsberichte der Königlich Preussischen Akademie der Wissenschaften zu Berlin*, 191-202.

El-Swaify S. A. and Emerson W. W. (1975) Changes in the physical properties of soil clays due to precipitated aluminum and iron hydroxides. I. Swelling and aggregate stability after drying. *Soil Sci. Soc. Am. Proc.* **39**, 1056-1063.

Epstein E. (1994) The anomaly of silicon in plant biology. *PNAS* **91**, 11-17.

Erhart H. (1963) Sur le cycle de la silice hydratée dans la biosphère. *C. R Acad. Sci. Paris* **256**, 3731-3734.

Eusterhues K., Neidhardt J., Hädrich A., Küsel K. and Totsche K. U. (2014) Biodegradation of ferrihydrite-associated organic matter. *Biogeochemistry* **119**, 45-50.

Eusterhues K., Rumpel C. and Kögel-Knabner I. (2005) Organo-mineral associations in sandy acid forest soils: importance of specific surface area, iron oxides and micropores. *Eur. J. Soil Sci.* **56**, 753-763.

Filimonova S., Kaufhold S., Wagner F. E., Häusler W. and Kögel-Knabner I. (2016) The role of allophane nano-structure and Fe oxide speciation for hosting soil organic matter in an allophanic Andosol. *Geochim. Cosmochim. Acta* **180**, 284-302.

Ford R., G. and Bertsch P. M. (1999) Distinguishing between surface and bulk dehydration-dehydroxylation reactions in synthetic goethites by high-resolution thermogravimetric analysis. *Clays Clay Miner.* **47**, 329-337.

Fraysse F., Pokrovsky O. S., Schott J. and Meunier J.-D. (2006) Surface properties, solubility and dissolution kinetics of bamboo phytoliths. *Geochim. Cosmochim. Acta* **70**, 1939-1951.

Fraysse F., Pokrovsky O. S., Schott J. and Meunier J.-D. (2009) Surface chemistry and reactivity of plant phytoliths in aqueous solutions. *Chem. Geol.* **258**, 197-206.

Frings P. J., Schubring F., Oelze M. and von Blanckenburg F. (2021) Quantifying biotic and abiotic Si fluxes in the critical zone with Ge/Si ratios along a gradient of erosion rates. *Am. J. Sci.* **321**, 1204-1245.

Harsh J., Chorover J. and Nizeyimana E. (2002) Allophane and imogolite. *Soil mineralogy with environmental applications* **7**, pp.291-322.

Haysom M. B. and Chapman L. S. (1975) Some aspects of the calcium silicate trials at Mackay. *Proc Conf Qld Soc Sugar Cane Technologists* **42**, 117-122.

Henmi I., Matsue N. and Henmi T. (1999) Dissolution and chemical changes of allophane and imogolite by dilute nitric acid solutions. *J Soil Sci Plant Nut* (*Japan*) **70**, 25-30.

Henmi I., Matsue N. and Henmi T. (2001) Effect of acid species and co-existing anions on the dissolution of Al and Si from allophane by the treatment of diluted acid solutions. *J. Ceram. Soc. JAPAN* **41**, 58-63.

Henriet C., Bodarwé L., Dorel M., Draye X. and Delvaux B. (2008) Leaf silicon content in banana (*Musa* spp.) reveals the weathering stage of volcanic ash soils in Guadeloupe. *Plant Soil* **313**, 71-82.

Henriet C., Draye X., Oppitz I., Swennen R. and Delvaux B. (2006) Effects, distribution and uptake of silicon in banana (*Musa* spp.) under controlled conditions. *Plant Soil* **287**, 359-374.

Hiemstra T. (2013) Surface and mineral structure of ferrihydrite. *Geochim. Cosmochim. Acta* **10**5, 316-325.

Hiemstra T. (2018) Ferrihydrite interaction with silicate and competing oxyanions: geometry and hydrogen bonding of surface species. *Geochim. Cosmochim. Acta* **238**, 453-476.

Hiemstra T., Barnett M. O. and van Riemsdijk W. H. (2007) Interaction of silicic acid with goethite. *J. Colloid Interface Sci.* **310**, 8-17.

Houba V. J. G., Temminghoff E. J. M., Gaikhorst G. A. and Van Vark W. (2000) Soil analysis procedures using 0.01 M calcium chloride as extraction reagent. C*ommun. Soil Sci. Plant Anal.* **31**, 1299-1396.

Houben D., Sonnet P. and Cornelis J.-T. (2014) Biochar from miscanthus: a potential silicon fertilizer. *Plant Soil* **374**, 871-882.

Houben G. and Kaufhold S. (2011) Multi-method characterization of the ferrihydrite to goethite transformation. *Clay Miner.* **46**, 387-395.

Huertas F. J., Chou L. and Wollast R. (1999) Mechanism of kaolinite dissolution at room temperature and pressure Part II: Kinetic study. *Geochim. Cosmochim. Acta* **63**, 3261-3275.

Irfan K., Trolard F., Shahzad T., Cary L., Mouret J. C. and Bourrié G. (2017) Impact of 60 years of intensive rice cropping on clay minerals in soils due to Si exportation. *Am. J. Agric. For*. **5**, 40.

Jambor J. L. and Dutrizac J. E. (1998) Occurrence and constitution of natural and synthetic ferrihydrite, a widespread iron oxyhydroxide. *Chem. Rev.* **98**, 2989-2990.

Johnston C. T. and Tombácz E. (2002) Surface chemistry of soil minerals. *Soil mineralogy with environmental applications* **7**, pp.37-67.

Jones D. L. and Willett V. B. (2006) Experimental evaluation of methods to quantify dissolved organic nitrogen (DON) and dissolved organic carbon (DOC) in soil. *Soil Biol. Biochem.* **38**, 991-999.

Jones L. H. P. and Handreck K. A. (1963) Effects of iron and aluminium oxides on silica in solution in soils. *Nature* **198**, 852-853.

Jouquet P., Jamoteau F., Majumdar S., Podwojewski P., Nagabovanalli P., Caner L., Barboni D. and Meunier J.-D. (2020) The distribution of silicon in soil is influenced by termite bioturbation in South Indian forest soils. *Geoderma* **372**, 114362.

Kaiser K. and Guggenberger G. (2007) Sorptive stabilization of organic matter by microporous goethite: sorption into small pores *vs* surface complexation. *Eur. J. Soil Sci*. **58**, 45-59.

Kameda J. (2021) Mineralogical and physico-chemical properties of halloysite-bearing slip surface material from a landslide during the 2018 Eastern Iburi earthquake, Hokkaido. *Prog. Earth Planet. Sci.* **8**, 1-13.

Karathanasis A. D. (2002) Mineral equilibria in environmental soil systems. *Soil mineralogy with environmental applications* **7**, pp.109-151.

Kaufhold S., Ufer K., Kaufhold A., Stucki J. W., Anastácio A. S., Jahn R. and Dohrmann R. (2010) Quantification of allophane from Ecuador. *Clays Clay Miner.* **58**, 707-716.

Kawamoto K., Yokoo H., Ochiai A., Nakano Y., Takeda A., Oki T., Takehara M., Uehara M., Fukuyama K., Ohara Y. and Ohnuki T. (2021) The role of nanoscale aggregation of ferrihydrite and amorphous silica in the natural attenuation of contaminant metals at mill tailings sites. *Geochim. Cosmochim. Acta* **298**, 207-226.

Kaya A. and Yukselen Y. (2005) Zeta potential of clay minerals and quartz contaminated by heavy metals. *Can. Geotech. J.* **42**, 1280-1289.

Keller C., Rizwan M. and Meunier J.-D. (2021) Are clay minerals a significant source of Si for crops? A comparison of amorphous silica and the roles of the mineral type and pH. *Silicon*, 1-8.

Kelly E. F. (1990) Methods for extracting opal phytoliths from soil and plant material. In: *Workshop on biotic indicators of global change*, Seatlle, Washington.

Kleber M., Eusterhues K., Keiluweit M., Mikutta C., Mikutta R. and Nico P. S. (2015) Mineral–organic associations: formation, properties, and relevance in soil environments. *Adv. Agron.* **130**, 1-140.

Kleber M., Mikutta R., Torn M. S. and Jahn R. (2005) Poorly crystalline mineral phases protect organic matter in acid subsoil horizons. *Eur. J. Soil Sci.* **56**, 717-725.

Koning E., Epping E. and Van Raaphorst W. (2002) Determining biogenic silica in marine samples by tracking silicate and aluminium concentrations in alkaline leaching solutions. *Aquat. Geochem.* **8**, 37-67.

Korndörfer G. H., Coelho N. M., Snyder G. H. and Mizutani C. T. (1999) Avaliação de métodos de extração de silício em sols cultivados com arroz de sequeiro. *Rev Bras Cienc Solo.* **23**, 101-106.

Kretzschmar R., Robarge W. P. and Weed S. B. (1993) Flocculation of kaolinitic soil clays: Effects of humic substances and iron oxides. *Soil Sci Soc Am J.* **57**, 1277-1283.

Kurtz A. and Derry L. (2004) Tracing silicate weathering and terrestrial silica cycling with Ge/ Si ratios. In: Wanty, R., Seal, R. (Eds.), *Proceeding of the 11th International Symposium on Water Rock Interaction*, the Netherlands, pp.833-836.

Kurtz A. C., Derry L. A. and Chadwick O. A. (2002) Germanium-silicon fractionation in the weathering environment. *Geochim. Cosmochim. Acta* **66**, 1525-1537.

Latrille C., Denaiz L. and Lamy I. (2003) Interaction of copper and zinc with allophane and organic matter in the B horizon of an Andosol. *Eur. J. Soil Sci.* **54**, 357-364.

Laugier E. J., Casana J. and Cabanes D. (2022) Phytolith evidence for the pastoral origins of multi-cropping in Mesopotamia (ancient Iraq). *Sci. Rep.* **12**.

Lehmann J. and Kleber M. (2015) The contentious nature of soil organic matter. *Nature* **528**, 60-68.

Li Z., Cornelis J.-T., Vander Linden C., Van Ranst E. and Delvaux B. (2020a) Neoformed aluminosilicate and phytogenic silica are competitive sinks in the silicon soil–plant cycle. *Geoderma* **368**, 114308.

Li Z., de Tombeur F., Vander Linden C., Cornelis J.-T. and Delvaux B. (2020b) Soil microaggregates store phytoliths in a sandy loam. *Geoderma* **360**, 114037.

Li Z., Unzué-Belmonte D., Cornelis J.-T., Vander Linden C., Struyf E., Ronsse F. and Delvaux B. (2019) Effects of phytolithic rice-straw biochar, soil buffering capacity and pH on silicon bioavailability. *Plant Soil* **438**, 187-203.

Lindsay W. L. (1979) *Chemical equilibria in soils*. John Wiley and Sons Ltd, Chichester, Sussex.

Lugolobi F., Kurtz A. C. and Derry L. A. (2010) Germanium–silicon fractionation in a tropical, granitic weathering environment. *Geochim. Cosmochim. Acta* **74**, 1294-1308.

Maeda T. and Warkentin B. P. (1975) Void changes in allophane soils deter- mining water retention and transmission. *Soil Sci. Soc. Am. Proc.* **39**, 398-403.

Meek K., Derry L., Sparks J. and Cathles L. (2016) $^{87}Sr/^{86}Sr$, Ca/Sr, and Ge/Si ratios as tracers of solute sources and biogeochemical cycling at a temperate forested shale catchment, central Pennsylvania, USA. *Chem. Geol.* **445**, 84-102.

Mestdagh M. M., Herbillon A. J., Rodrique L. and Rouxhet P. G. (1982) Evaluation du rôle du fer structural sur la cristallinité des kaolinites. *Bull. Mineral.* **105**, 457-466.

Meunier J.-D. (2003) Le rôle des plantes dans le transfert du silicium à la surface des continents. *C. R -Geosci.* **335**, 1199-1206.

Meunier J.-D., Keller C., Guntzer F., Riotte J., Braun J. J. and Anupama K. (2014) Assessment of the 1% Na_2CO_3 technique to quantify the phytolith pool. *Geoderma* **216**, 30-35.

Monger H. C. and Kelly E. F. (2002) Silica minerals. *Soil mineralogy with environmental applications* **7**, 611-636.

Murnane R. J. and Stallard R. F. (1990) Germanium and silicon in rivers of the Orinoco drainage basin. *Nature* **344**, 749-752.

Nawaz M. A., Zakharenko A. M., Zemchenko I. V., Haider M. S., Ali M. A., Imtiaz M., Chung G., Tsatsakis A., Sun S. and Golokhvast K. S. (2019) Phytolith formation in plants: from soil to cell. *Plants* **8**, 249.

Nguyen A. T., Nguyen A. M., Nguyen L. N., Nguyen H. X., Tran T. M., Tran P. D., Dultz S. and Nguyen M. N. (2021) Effects of CO_2 and temperature on phytolith dissolution. *Sci. Total Environ.* **772**, 145469.

Nguyen M., Dultz S. and Guggenberger G. (2014) Effects of pretreatment and solution chemistry on solubility of rice-straw phytoliths. *J. Plant. Nutr. Soil Sci.* **177**, 349-359.

Ohashi F., Wada S.I., Suzuki M., Maeda M. and Tomura S. (2002) Synthetic allophane from high concentration solutions: nanoengineering of the porous solid. *Clay Miner.* **37**, 451-456.

Opfergelt S., Cardinal D., André L., Delvigne C., Bremond L. and Delvaux B. (2010) Variations of $\delta^{30}Si$ and Ge/Si with weathering and biogenic input in tropical basaltic ash soils under monoculture. *Geochim. Cosmochim. Acta* **74**, 225-240.

Pačes T. (1978) Reversible control of aqueous aluminum and silica during the irreversible evolution of natural waters. *Geochim. Cosmochim. Acta* **42**, 1487-1493.

Parfitt R. L. (2009) Allophane and imogolite: role in soil biogeochemical processes. *Clay Miner.* **44**, 135-155.

Parfitt R. L., Childs C. W. and Eden D. N. (1988) Ferrihydrite and allophane in four Andepts from Hawaii and implications for their classification. *Geoderma* **41**, 223-241.

Perez-Fodich A. and Derry L. A. (2020) A model for germanium-silicon equilibrium fractionation in kaolinite. *Geochim. Cosmochim. Acta* **288**, 199-213.

Pinheiro-Dick D. and Schwertmann U. (1996) Microaggregates from Oxisols and Inceptisols: dispersion through selective dissolutions and physicochemical treatments. *Geoderma* **74**, 49-63.

Piperno D. R. (1988) Phytolith analysis, an archaeological and geological perspective. San Diego: Academic Press.

Puppe D. and Leue M. (2018) Physicochemical surface properties of different biogenic silicon structures: Results from spectroscopic and microscopic analyses of protistic and phytogenic silica. *Geoderma* **330**, 212-220.

Puppe D., Höhn A., Kaczorek D., Wanner M., Wehrhan M. and Sommer M. (2017) How big is the influence of biogenic silicon pools on short-term changes in water-soluble silicon in soils? Implications from a study of a 10-year-old soil–plant system. *Biogeosciences* **14**, 5239-5252.

Qi H. W., Hu R. Z., Jiang K., Zhou T., Liu Y. F. and Xiong Y. W. (2019) Germanium isotopes and Ge/Si fractionation under extreme tropical weathering of basalts from the Hainan Island, South China. *Geochim. Cosmochim. Acta* **253**, 249-266.

Quigley K. M., Donati G. L. and Anderson T. M. (2017) Variation in the soil 'silicon landscape' explains plant silica accumulation across environmental gradients in Serengeti. *Plant Soil* **410**, 217-229.

Ralston S. J., Hausrath E. M., Tschauner O., Rampe E., Peretyazhko T. S., Christoffersen R., Defelice C. and Lee H. (2021) Dissolution rates of allophane with variable Fe contents: Implications for aqueous alteration and the preservation of X-ray amorphous materials on Mars. *Clays Clay Miner.* 1-26.

Russell M., Parfitt R. L. and Claridge G. G. C. (1981) Estimation of the amounts of allophane and other materials in the clay fraction of an Egmont loam profile and other volcanic ash soils, New Zealand. *Soil Res.* **19**, 185-195.

Saccone L., Conley D. and Sauer D. (2006) Methodologies for amorphous silica analysis. *J. Geochem. Explor.* **88**, 235-238.

Saccone L., Conley D. J., Koning E., Sauer D., Sommer M., Kaczorek D., Blecker S. W. and Kelly E. F. (2007) Assessing the extraction and quantification of amorphous silica in soils of forest and grassland ecosystems. *Eur. J. Soil Sci.* **58**, 1446-1459.

Sanchez P. A. (2019) *Properties and management of soils in the tropics*. Cambridge University Press.

Sauer D., Saccone L., Conley D. J., Herrmann L. and Sommer M. (2006) Review of methodologies for extracting plant-available and amorphous Si from soils and aquatic sediments. *Biogeochemistry* **80**, 89-108.

Schofield R. K. and Samson H. R. (1954) Flocculation of kaolinite due to the attraction of oppositely charged crystal faces. *Discuss. Faraday Soc.* **18**, 135-145.

Seyfferth A. L., Kocar B. D., Lee J. A. and Fendorf S. (2013) Seasonal dynamics of dissolved silicon in a rice cropping system after straw incorporation. *Geochim. Cosmochim. Acta* **123**, 120-133.

Six J., Conant R., Paul E. A. and Paustian K. (2002) Stabilization mechanisms of soil organic matter: implications for C-saturation of soils. *Plant Soil* **241**, 155-176.

Six J., Paustian K., Elliott E. T. and Combrink C. (2000) Soil structure and organic matter: I. Distribution of aggregate-size classes and aggregate-associated carbon. *Soil Sci Soc Am J.* **64**, 681-689.

Sposito G. (2016) *The chemistry of soils*, 3rd edition. Oxford University Press, New York, NY.

Strömberg C. A., Dunn R. E., Crifò C. and Harris E. B. (2018) Phytoliths in paleoecology: analytical considerations, current use, and future directions. In *Methods in Paleoecology*, pp.235-287. Springer, Cham.

Su C. and Harsh J. B. (1993) The electrophoretic mobility of imogolite and allophane in the presence of inorganic anions and citrate. *Clays Clay Miner.* **41**, 461-471.

Su C. and Harsh J. B. (1998) Dissolution of allophane as a thermodynamically unstable solid in the presence of boehmite at elevated temperatures and equilibrium vapor pressures. *Soil Sci.* **163**, 299-312.

Tombácz E. and Meleg E. (1990) A theoretical explanation of the aggregation of humic substances as a function of pH and electrolyte concentration. *Org. Geochem.* **15**, 375-382.

Tombácz E., Libor Z., Illés E., Majzik A. and Klumpp E. (2004) The role of reactive surface sites and complexation by humic acids in the interaction of clay mineral and iron oxide particles. *Org. Geochem.* **35**, 257-267.

Totsche K. U., Amelung W., Gerzabek M. H., Guggenberger G., Klumpp E., Knief C., Lehndorff E., Mikutta R., Peth S., Prechte A., Ray N. and Kögel-Knabner I. (2018) Microaggregates in soils. *J. Plant. Nutr. Soil Sci.* **181**, 104-136.

Trinh T. K., Nguyen T. T., Nguyen T. N., Wu T. Y., Meharg A. A. and Nguyen M. N. (2017) Characterization and dissolution properties of phytolith occluded phosphorus in rice straw. *Soil Tillage Res.* **171**, 19-24.

Van Wambeke A. (1992) Soils of the tropics: properties and appraisal. *McGraw Hill*.

Vander Linden C. and Delvaux B. (2019) The weathering stage of tropical soils affects the soil-plant cycle of silicon, but depending on land use. *Geoderma* **351**, 209-220.

Vander Linden C., Li Z., Iserentant A., Van Ranst E., de Tombeur F. and Delvaux B. (2021) Rainfall is the major driver of plant Si availability in perudic gibbsitic Andosols. *Geoderma* **404**, 115295.

Vandevenne F. I., Barão L., Ronchi B., Govers G., Meire P., Kelly E. F. and Struyf E. (2015) Silicon pools in human impacted soils of temperate zones. *Global Biogeochem Cycles* **29**, 1439-1450.

Violette A., Goddéris Y., Maréchal J. C., Riotte J., Oliva P., Kumar M. S. M., Sekhar M. and Braun J. J. (2010) Modelling the chemical weathering fluxes at the watershed scale in the tropics (Mule Hole, South India): Relative contribution of the smectite/kaolinite assemblage versus primary minerals. *Chem. Geol.* **277**, 42-60.

Wang S., Du P., Yuan P., Liu Y., Song H., Zhou J., Deng L. and Liu D. (2020) Structural alterations of synthetic allophane under acidic conditions: Implications for understanding the acidification of allophanic Andosols. *Geoderma* **376**, 114561.

Warkentin B. P. and Maeda T. (1980) Physical and mechanical characteristics of Andisols. In: Then, B.K.G. (Ed.), *Soils with variable charge*. New Zealand Society of Soil Science, Lower Hutt, pp. 281-301.

Wei S., Tan W., Zhao W., Yu Y., Liu F. and Koopal L. K. (2012) Microstructure, interaction mechanisms, and stability of binary systems containing goethite and kaolinite. *Soil Sci Soc Am J.* **76**, 389-398.

West S. L., White G. N., Deng Y., McInnes K. J., Juo A. S. R. and Dixon J. B. (2004) Kaolinite, halloysite, and iron oxide influence on physical behavior of formulated soils. *Soil Sci Soc Am J.* **68**, 1452-1460.

White G. N. and Dixon J. B. (2002) Kaolin–serpentine minerals. *Soil mineralogy with environmental applications* **7**, pp.389-414.

White, A. F., Vivit, D. V., Schulz, M. S., Bullen, T. D., Evett, R. R. and Aagarwal, J. (2012) Biogenic and pedogenic controls on Si distributions and cycling in grasslands of the Santa Cruz soil chronosequence, California. *Geochim. Cosmochim. Acta* **94**, 72-94.

Wieland E. and Stumm W. (1992) Dissolution kinetics of kaolinite in acidic aqueous solutions at 25 °C. *Geochim. Cosmochim. Acta* **56**, 3339-3355.

Xie Z. and Walther J. V. (1992) Incongruent dissolution and surface area of kaolinite. *Geochim. Cosmochim. Acta* **56**, 3357-3363.

Yang L. and Steefel C. I. (2008) Kaolinite dissolution and precipitation kinetics at 22 °C and pH 4. *Geochim. Cosmochim. Acta* **72**, 99-116.

Yang X., Song Z., Qin Z., Wu L., Yin L., Van Zwieten L., Song A., Ran X., Yu C. and Wang H. (2020) Phytolith-rich straw application and groundwater table management over 36 years affect the soil-plant silicon cycle of a paddy field. *Plant Soil* **454**, 343-358.

Yoshida S. (1981) *Fundamentals of rice crop science*. International Rice Research Institute, Los Baños, Laguna, Philippines.

Yvon J., Liétard O., Cases J. M. and Delon J. F. (1982) Minéralogie des argiles kaoliniques des Charentes. *Bull. Minéral.* **105**, 431-437.

Table 1. Total concentrations of Si, Al and Ge, Si/Al and Ge/Si molar ratio in the individual components allophane, kaolinite, phytolith and quartz, and in *Am* and *Cryst* bulk mixtures.

	Si	Al	Ge	Si/Al	Ge/Si
	g kg^{-1}		µg kg^{-1}	mol mol^{-1}	µmol mol^{-1}
allophane	116.79	156.02	283.53	0.72	0.94
kaolinite	204.10	197.98	2302.92	0.99	4.36
phytolith	381.29	nd*	403.07	nd	0.41
quartz	444.11	nd	2419.41	nd	2.10
bulk mixture (*Am*)	271.73	52.57	1319.84	4.96	1.87
bulk mixture (*Cryst*)	305.44	73.20	2038.06	4.00	2.58

*nd: not detected

Table 2. Specific surface area (SSA), as measured after degassing at 200, 100 and 40 °C, and zeta potential of the individual components used in mixtures and aggregates: rice phytolith, synthesized allophane, ferrihydrite and goethite, kaolinite and quartz.

		phytolith	allophane	ferrihydrite	goethite	kaolinite	quartz
SSA (BET) (m^2 g^{-1})	degassing at 200 °C	190	306	242	132	24	1
	degassing at 100 °C		255	264	35		
	degassing at 40 °C		231	245			
zeta potential (mV)		–27.3	36.9	21.3	29.6	–28.2	–31.5
pH_{H2O}*		4.19	3.73	3.85	6.52	4.02	4.97
Conductivity (µs cm^{-1})*		0.06	0.45	0.01	0.03	0.07	0.01

* pH-H_2O and conductivity as determined in each suspension (10 mg : 10 ml) used to measure zeta potential.

Table 3. Estimated contents of amorphous Si (ASi) and Al (AAl), as quantified following DeMaster (1981) from Na_2CO_3 extractable Si (Na_2CO_3-Si) and Al (Na_2CO_3-Al) concentrations, and their Si/Al molar ratio, in phytolith, allophane, kaolinite, mixtures and aggregates of the amorphous (*Am*) and crystalline (*Cryst*) models. Different lowercase letter (a, b) resulting from the independent samples *t*–separation test is given to compare unaggregated mixtures with aggregates ($p < 0.05$). *Note*: Na_2CO_3-Si was 0 g kg^{-1} in OM and quartz, Na_2CO_3-Al was not detected in phytoliths (see Fig. S2 and S3).

	ASi (g kg^{-1})		AAl (g kg^{-1})		Si/Al (mol mol^{-1})
	mean	s.d	mean	s.d	
phytolith	271.91	15.63	nd*	nd	nd
allophane	43.69	5.29	87.45	6.85	0.5
kaolinite	1.16	0.04	0.98	0.12	1.1
quartz	nd		nd		nd
OM	nd		nd		nd
Am mixtures	22.4a	2.80	28.83a	4.51	0.76b
Am aggregates	15.30b	2.88	13.94b	3.24	1.05a
Cryst mixtures	9.01a	0.42	0.76a	0.08	11.4b
Cryst aggregates	6.26b	0.55	0.11b	0.03	54.6a

* nd: not detected

Table 4. Concentrations of Si, Al and Ge, Si/Al and Ge/Si molar ratio in 0.01 M $CaCl_2$ extracts at 16 hours and 64 days for the individual components allophane, kaolinite, phytolith and quartz (a, b), and for the *Am* and *Cryst* mixtures and aggregates (c, d). Different lowercase letters a and b, resulting from the independent samples *t*–separation test, are given to compare parameters measured in mixtures and aggregates ($p < 0.05$). The pH values of the $CaCl_2$ extracts (pH_{CaCl2}) are also given.

		Si	Al	Ge	Si/Al	Ge/Si	pH_{CaCl2}
		g kg^{-1}		µg kg^{-1}	mol mol^{-1}	µmol mol^{-1}	
(a) $CaCl_2$ extract at 16 h	allophane	7.95	9.27	27.03	0.82	1.31	3.72
	kaolinite	0.01	0.01	0.64	0.96	24.74	3.69
	phytolith	0.21	nd	1.71	nd	3.15	3.59
	quartz	0.001	nd	nd	nd	nd	5.87
(b) $CaCl_2$ extract at 64 d	allophane	29.06	23.51	49.94	1.18	0.66	4.01
	kaolinite	0.15	0.02	0.71	7.2	1.83	3.58
	phytolith	5.62	nd	3.95	nd	0.27	3.56
	quartz	0.02	nd	nd	nd	nd	4.41
(c) $CaCl_2$ extract at 16 h	mixtures (*Am*)	0.33a	0.53a	0.34b	0.60a	0.40b	4.00
	aggregates (*Am*)	0.27b	0.35b	0.45a	0.74a	0.64a	3.97
	mixtures (*Cryst*)	0.06a	0.01a	0.99a	5.76b	6.37a	5.06
	aggregates (*Cryst*)	0.11a	0.00b	0.30b	358.12a	1.05b	6.78
(d) $CaCl_2$ extract at 64 d	mixtures (*Am*)	3.72a	3.65a	1.99a	0.98a	0.21b	4.41
	aggregates (*Am*)	0.95b	2.13b	1.91a	0.43b	0.77a	4.98
	mixtures (*Cryst*)	0.48a	0.00a	1.59a	959.14a	1.28a	7.31
	aggregates (*Cryst*)	0.39b	0.00a	0.51b	860.11b	0.50b	7.83

*nd: not detected

Table 5. Release rates of Si (RR-Si) from rice phytolith, kaolinite and allophane (this study), as compared to dissolution rates of other phytoliths (Fraysse *et al*., 2009) and synthetic allophane (Ralston *et al*., 2021). Si/Al ratio and BET SSA, as measured after degassing at 200 °C, of kaolinite and allophanes. Experimental conditions during Si release: pH range, temperature (T), solid:liquid ratio, extracting solution.

	allophane[1]	phytolith[1]	kaolinite[1]	allophane[2]	phytolith[3]
RR-Si (mol m^{-2} d^{-1}) x 10^6	59.9	4.8	1.1	1.1	1.1
Si/Al	0.77	-	0.99	1.0	1.0
BET SSA (m^2 g^{-1})	306	190	24	385	92-316
pH	3.7-4.0	3.6	36-3.7	3.2-4.1	3.0-3.9
T (°C)		20		25	25
Solid:liquid ratio[4] (g:ml)		2:20		0.15:180	0.2-0.5:30
Extracting solution		0.01M $CaCl_2$*		0.01 M NaCl†	0.01M NaCl‡

[1] This study (synthetic allophane, rice phytolith, *Charentes* kaolinite,).
[2] Ralston *et al*., 2021 (synthetic allophane).
[3] Fraysse *et al*., 2009 (horsetail, larch, elm and fern phytoliths).
[4] The RR-Si values were measured after extractions in plastic centrifuge tubes continuously shaken (this study), in acid-washed 250 mL polypropylene bottles continuously shaken (Ralston *et al.*, 2021), and in continuously stirred mixed flow 30-ml reactors plunged in a thermostatic water-bath at 25 °C (Fraysse *et al.*, 2009).
* Unbuffered solution. † pH adjusted with HNO_3. ‡ pH adjusted with HCl.

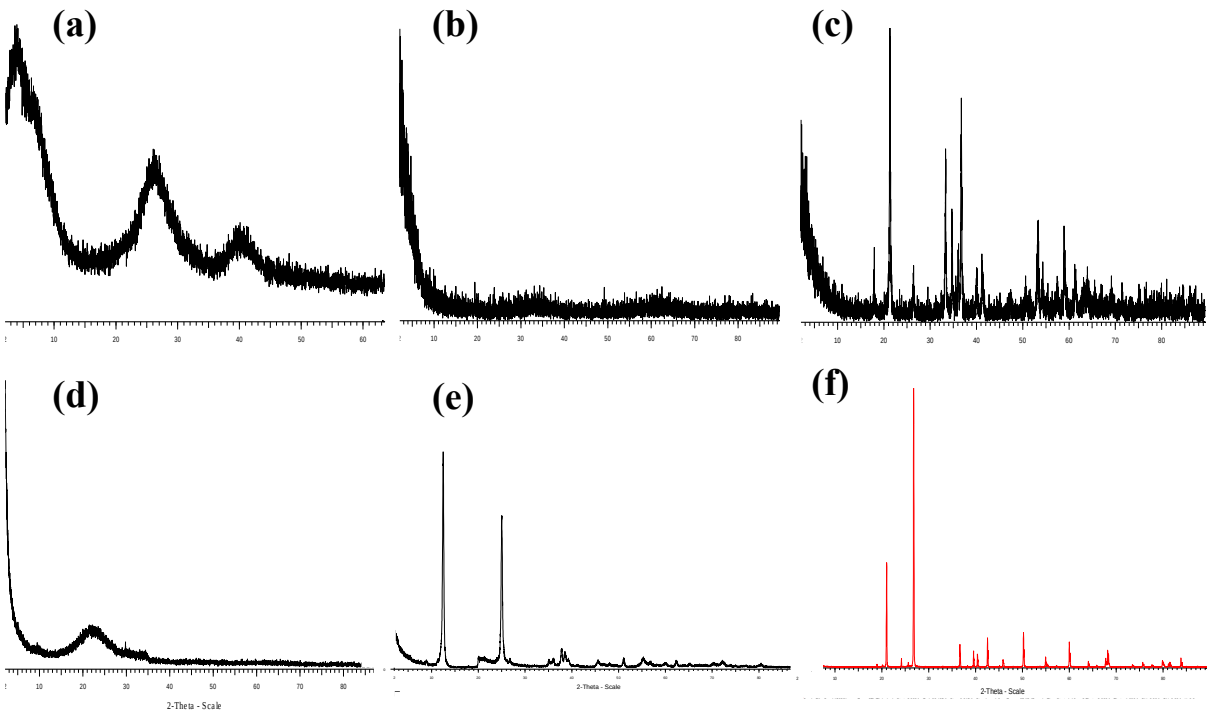

Figure 1. X-ray diffraction (XRD, Cu*K*α) patterns performed on freeze-dried, powdered samples: (a) allophane, (b) ferrihydrite, (c) goethite, (d) rice phytolith, (e) kaolinite, and (f) quartz.

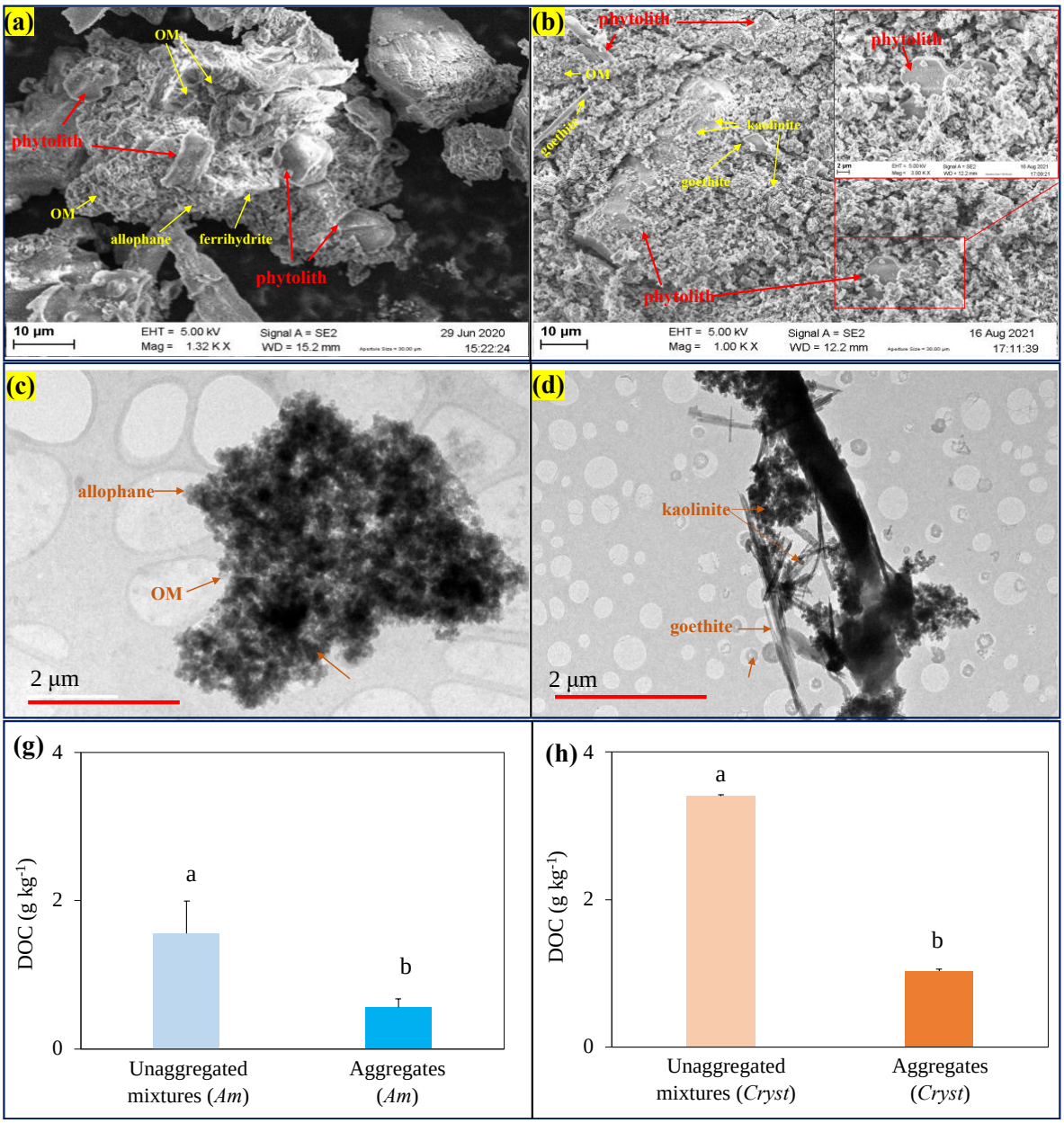

Figure 2. (a-b) SEM micrographs performed on aggregates (< 2 mm) of the (a) amorphous (*Am*) and (b) crystalline (*Cryst*) models (red arrows point to phytolith particles, yellow ones to other constituents). (c-d) TEM micrographs performed on aggregates (< 250 µm) of the (c) *Am* model, (d) *Cryst* model. (e-f) Dissolved organic carbon (DOC) as extracted by $CaCl_2$ 0.01M after 16h from the (g) *Am* and (h) *Cryst* mixtures and aggregates: different lowercase letters (a, b), resulting from the independent samples t–separation test, mean a significant difference between the mixture and aggregate at $p < 0.05$ in each model.

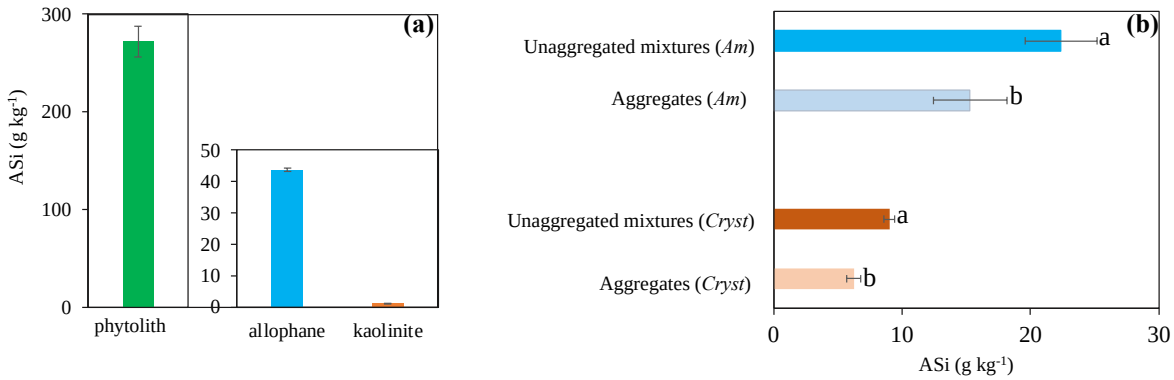

Figure 3. Estimated contents of amorphous Si (ASi), as quantified following *DeMaster* (1981) from Na_2CO_3 extractable Si (Na_2CO_3-Si) data (Fig. S2 and S3), in phytolith, allophane, kaolinite, mixtures and aggregates of the amorphous (*Am*) and crystalline (*Cryst*) models.

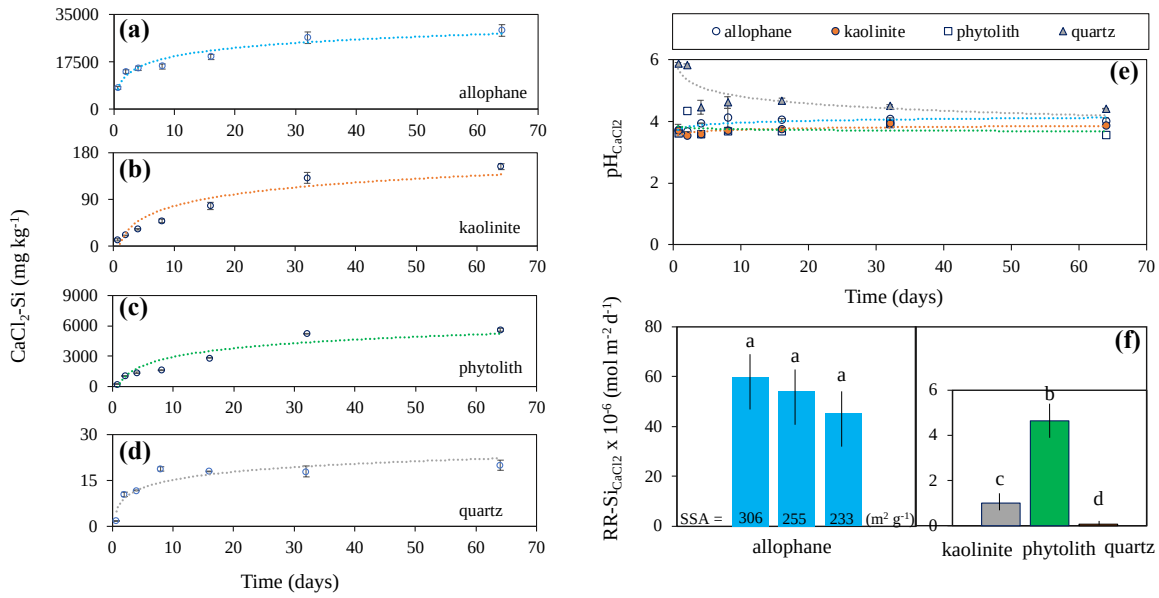

Figure 4. Time evolution (16 h to 64 d) of (a-d) Si concentration in the 0.01 M $CaCl_2$ extract ($CaCl_2$-Si) and of (e) pH_{CaCl2} for individual components (allophane, kaolinite, rice phytolith and quartz), as well as (f) the release rate of $CaCl_2$-Si from allophane, kaolinite, phytolith, and quartz. In Fig.5(f), different lower-case letters indicate a significant difference among allophane, kaolinite, phytolith and quartz, not between the three estimations for allophane for which the release rate of Si in $CaCl_2$ ($RR\text{-}Si_{CaCl2}$) was calculated using the three SSA values ($p < 0.05$, Tukey's mean separation test). *Note*: Both Si and Al were not detected in OM, while Al was not detected in both rice phytolith and quartz (see Fig.S4 in supplementary information).

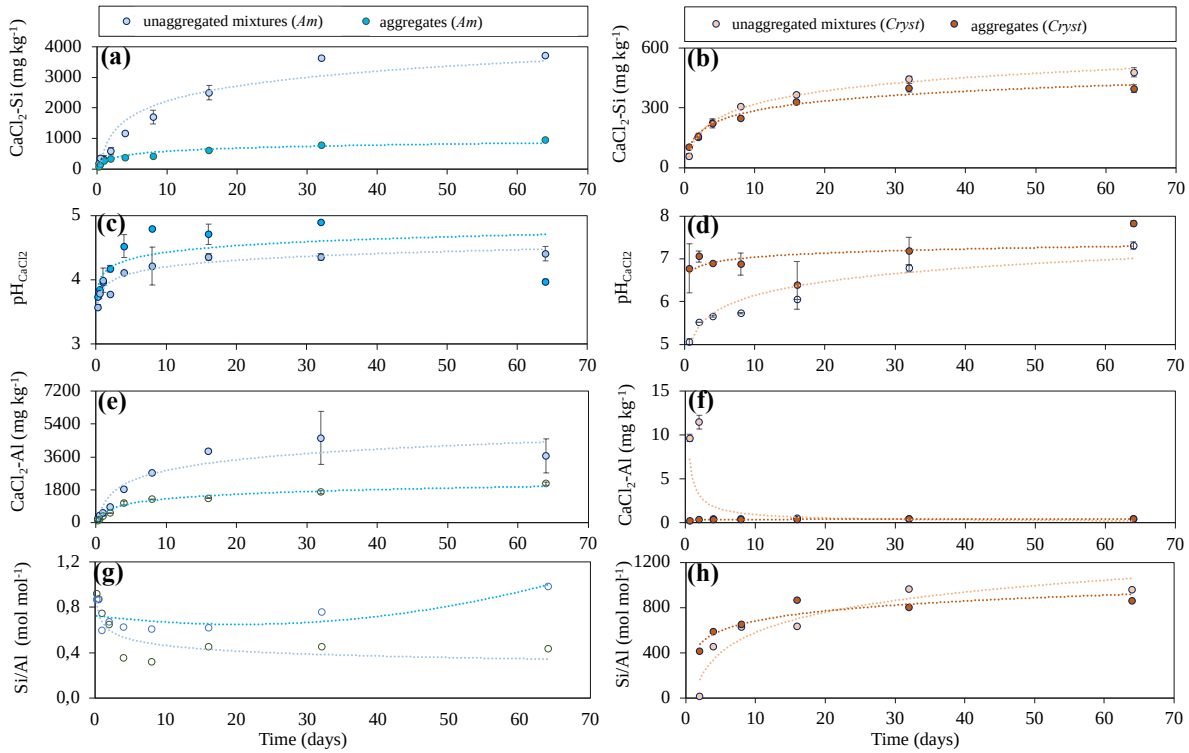

Figure 5. Time evolution, in the 0.01 M $CaCl_2$ extract, of (a-b) Si concentration ($CaCl_2$–Si), (c-d) pH (pH_{CaCl2}), (e-f) Al concentration ($CaCl_2$–Al), and (g, h) Si/Al ratio in unaggregated mixtures and aggregates of (left) the amorphous (*Am*) and (right) crystalline (*Cryst*) models.

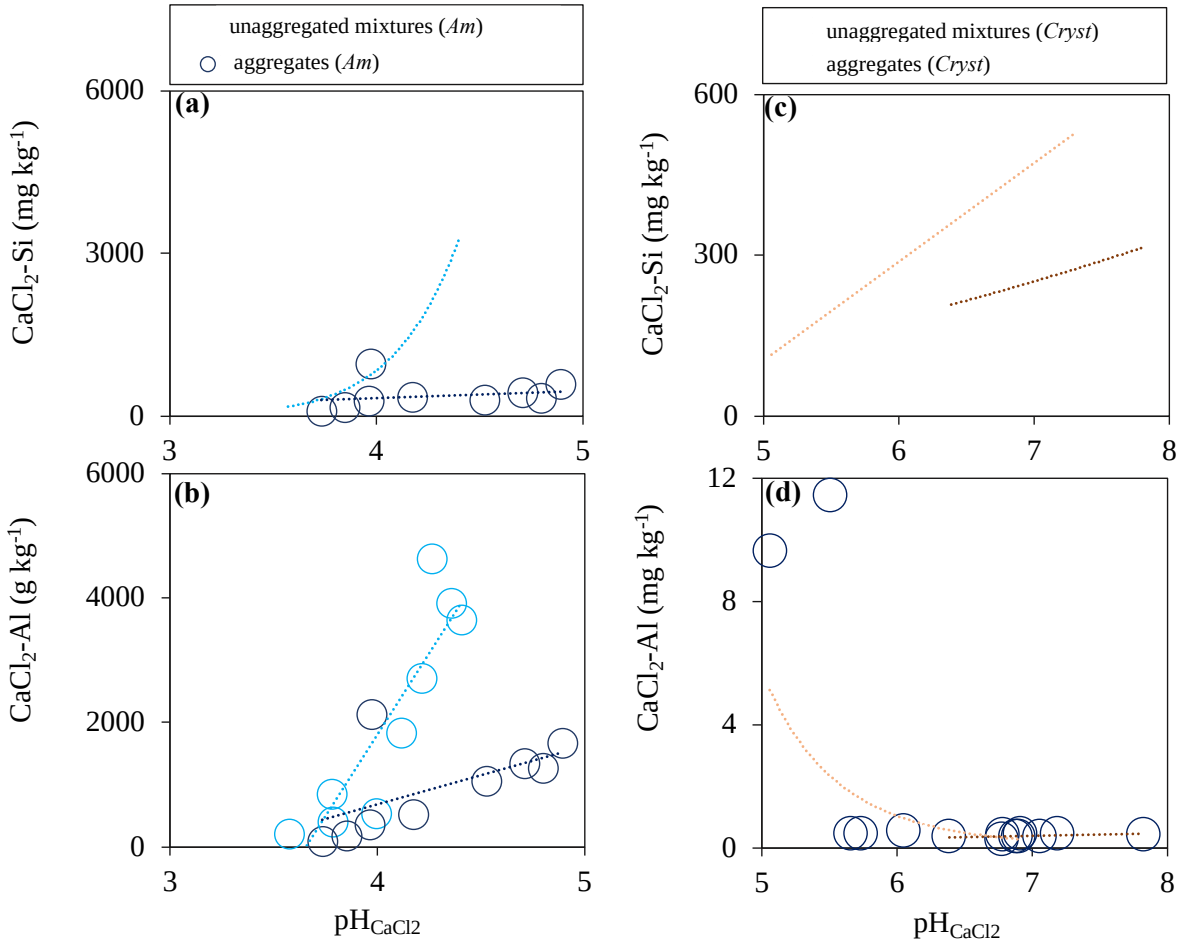

Figure 6. Concentrations of Si and Al in the $CaCl_2$ extracts ($CaCl_2$–Si and $CaCl_2$–Al) as plotted against pH of respective $CaCl_2$ extracts (pH_{CaCl2}) in (a-b) the unaggregated mixtures and aggregates of the amorphous (*Am*) model, (c-d) the unaggregated mixtures and aggregates of the crystalline (*Cryst*) model.

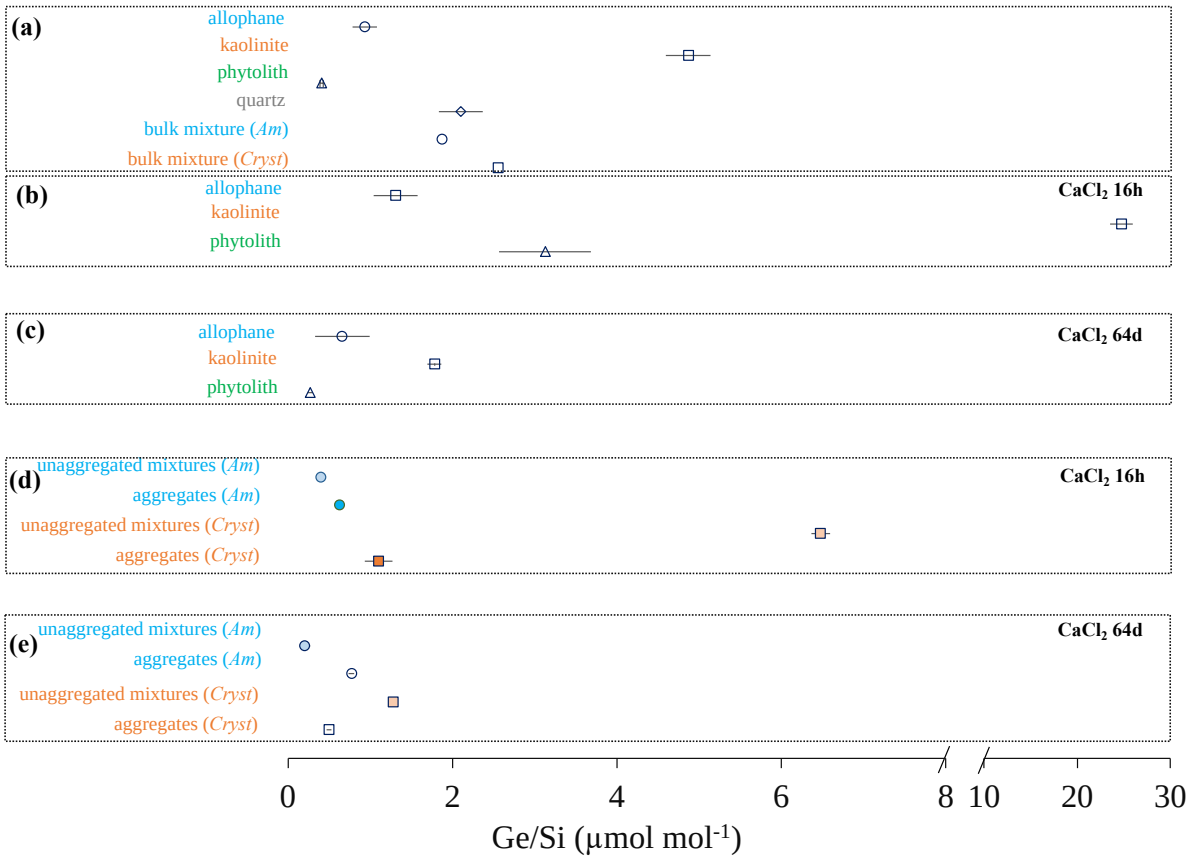

Figure 7. Values of the molar ratio Ge/Si (µmol mol^{-1}) of (a) the individual components allophane, kaolinite, phytolith, quartz and their bulk mixtures with OM and Fe oxide, (b-e) in the 0.01M $CaCl_2$ extracts for allophane, kaolinite and phytolith at (b) 16h and (c) 64d, and for the unaggregated mixtures and aggregates of both amorphous (*Am*) and crystalline (*Cryst*) models at (d) 16h and (e) 64d.

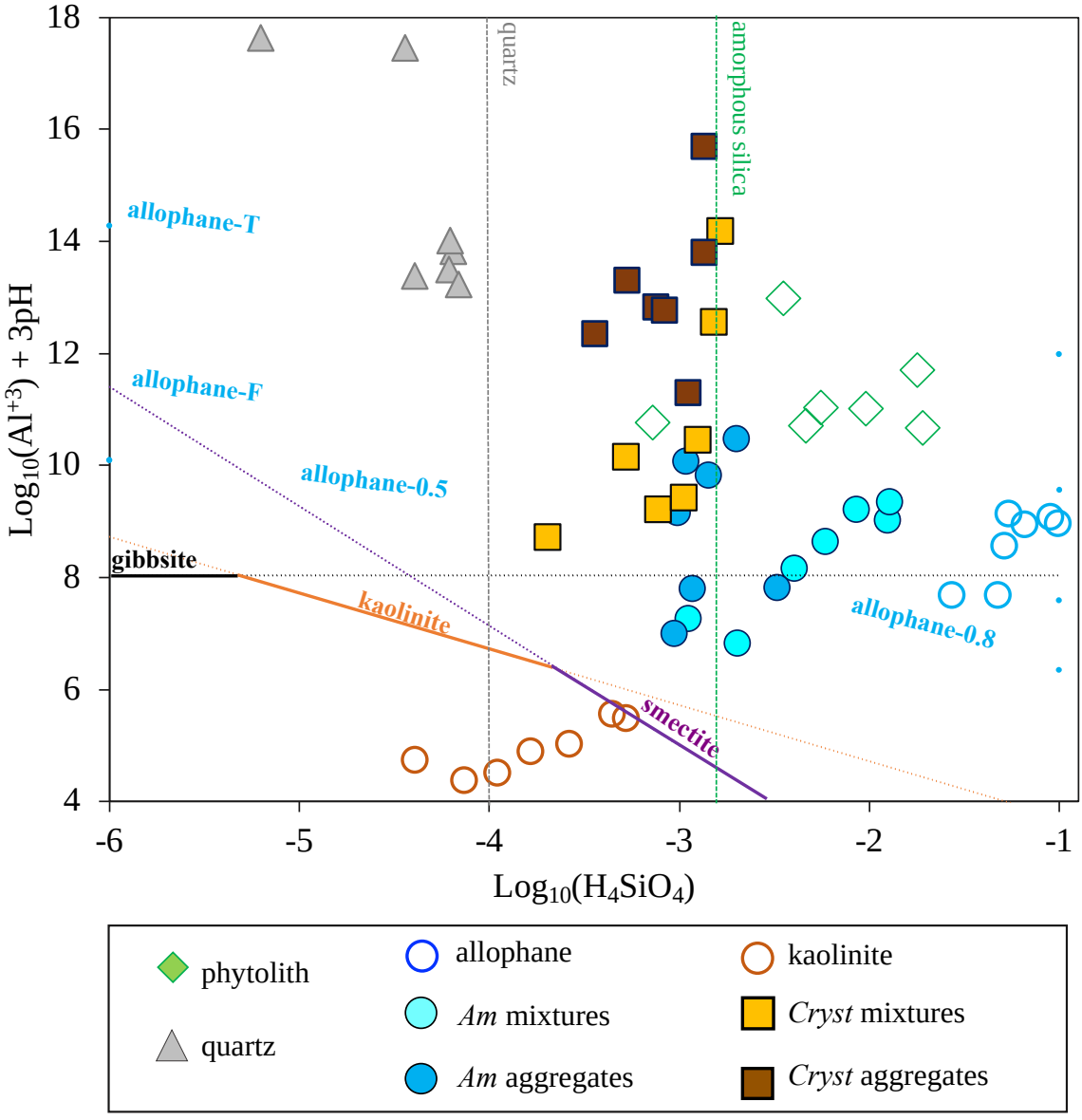

Figure 8. Plot of the logarithmic values of experimental Al^{3+}, H^+ and H_4SiO_4 concentrations (mol l^{-1}) in $CaCl_2$ extracts at each kinetic step (this study) in the stability diagram for reference allophane, gibbsite, kaolinite and smectite in the Al_2O_3–SiO_2–H_2O system. *Allophane-T* refers to theoretical composition calculated with amorphous silica and amorphous alumina as end-members, and might be regarded as a freshly precipitated amorphous aluminosilicate phase (Dobrzyński, 2006). *Allophane-F* refers to field data from Pačes (1978). *Allophane-0.5* and *allophane-0.8* refer to data on synthetic allophanes with Si/Al ratio of 0.5 and 0.8, respectively (Su and Harsh, 1998). Gibbsite, kaolinite and smectite solubility lines refer to Lindsay (1979).

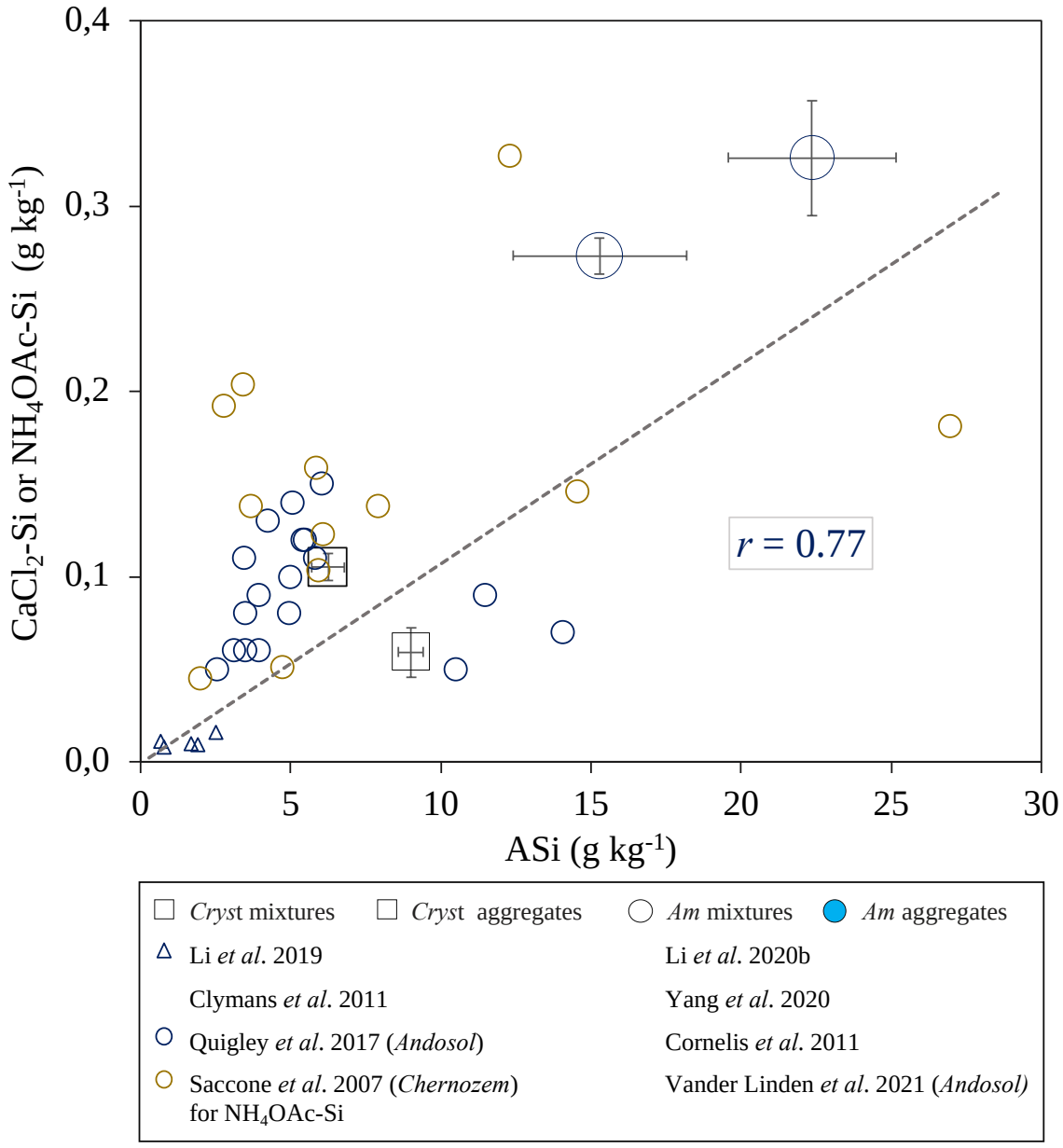

Figure 9. Plot of bioavailable Si content, as assessed by $CaCl_2$ 0.01 M or NH_4OAc 0.5 M, against amorphous Si content (ASi), as assessed by Na_2CO_3 (DeMaster, 1981), in soil samples from different soil–plant systems, and in the *Am* and *Cryst* mixtures and aggregates of this study. Note: NH_4OAc-Si only concerns the Chernozem samples (Saccone *et al*., 2007).

APPENDIX A Supporting Information for

Aggregation reduces the release of bioavailable silicon from allophane and phytolith

Zimin Li[‡,*], Jean-Dominique Meunier[†], Bruno Delvaux[‡]

[‡] Earth and Life Institute, Soil Science, Université catholique de Louvain (UCLouvain), Croix du Sud 2, L7.05.10, 1348 Louvain-La-Neuve, Belgium.

[†] CNRS, CEREGE, Aix Marseille Université, 13545 Aix-en-Provence Cedex 04, France.

[*]**Corresponding author:** zimin.li@uclouvain.be (Zimin Li)

Address: Earth and Life Institute, Soil sciences, Université catholique de Louvain (UCLouvain), Croix du Sud 2 / L7.05.10, 1348 Louvain-la-Neuve, Belgium.

Submitted to the journal of Geochimica et Cosmochimica Acta

Contents of this file:

Figures S1 to S4

Tables S1 to S2

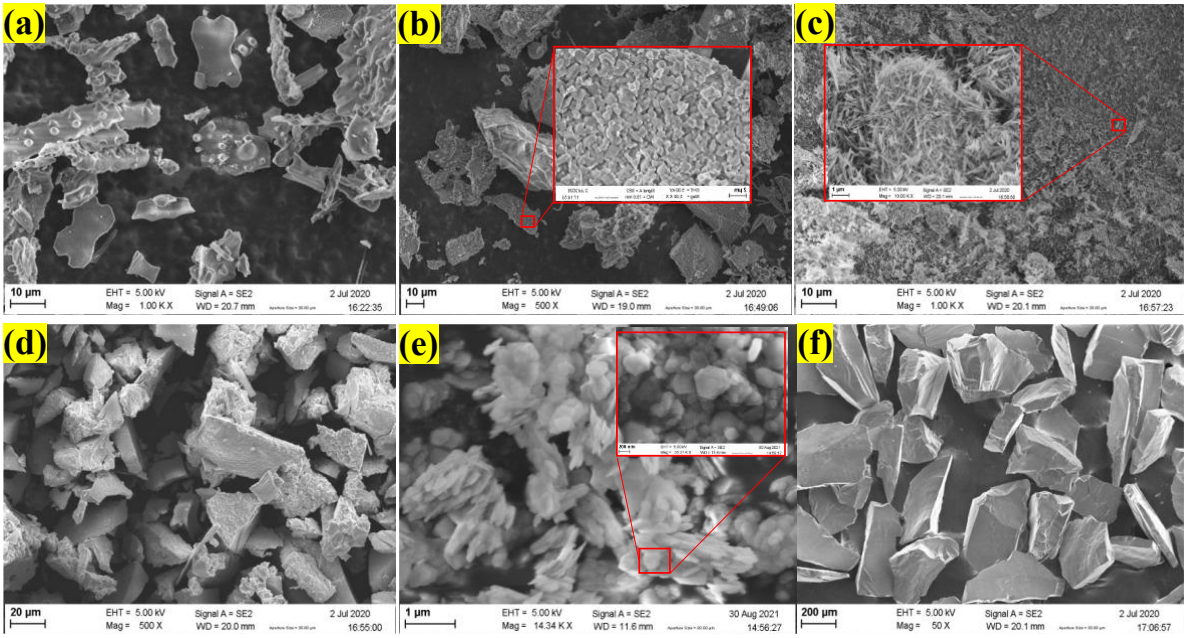

Figure S1. Scanning electron microscope (SEM) images of: (a) rice phytolith, (b) allophane, (c) goethite, (c) ferrihydrite, (e) kaolinite, and (f) quartz.

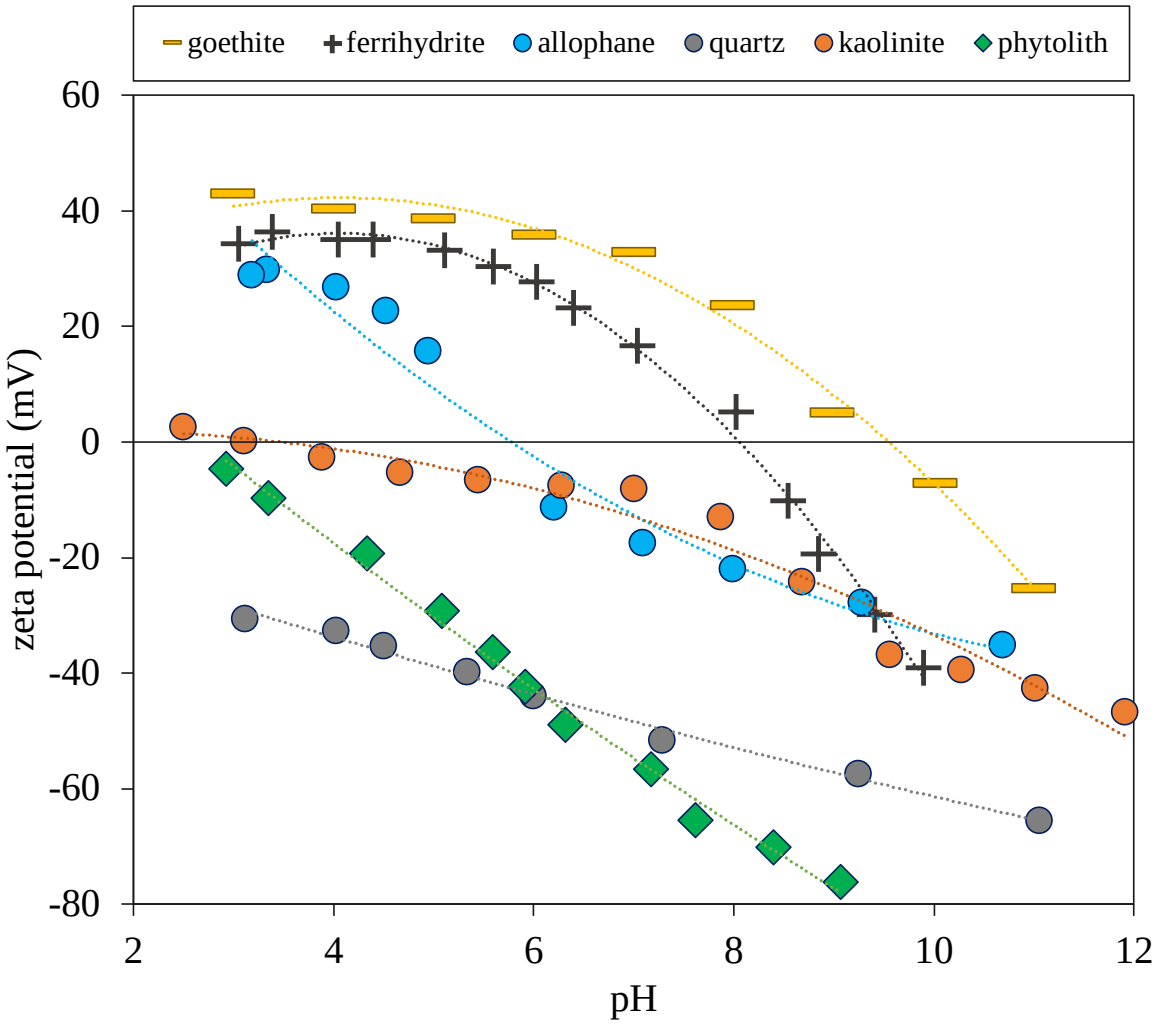

Figure S2. Variation of zeta potential in the pH range 2-12 for individual components used in mixtures and aggregates, as compiled from experimental data published in the literature: phytolith (Nguyen et al., 2014), allophane (Kameda, 2021), ferrihydrite (Kawamoto et al., 2021), goethite (Hiemstra et al., 2007), kaolinite (Au et al., 2015), quartz (Kaya and Yukselen, 2005).

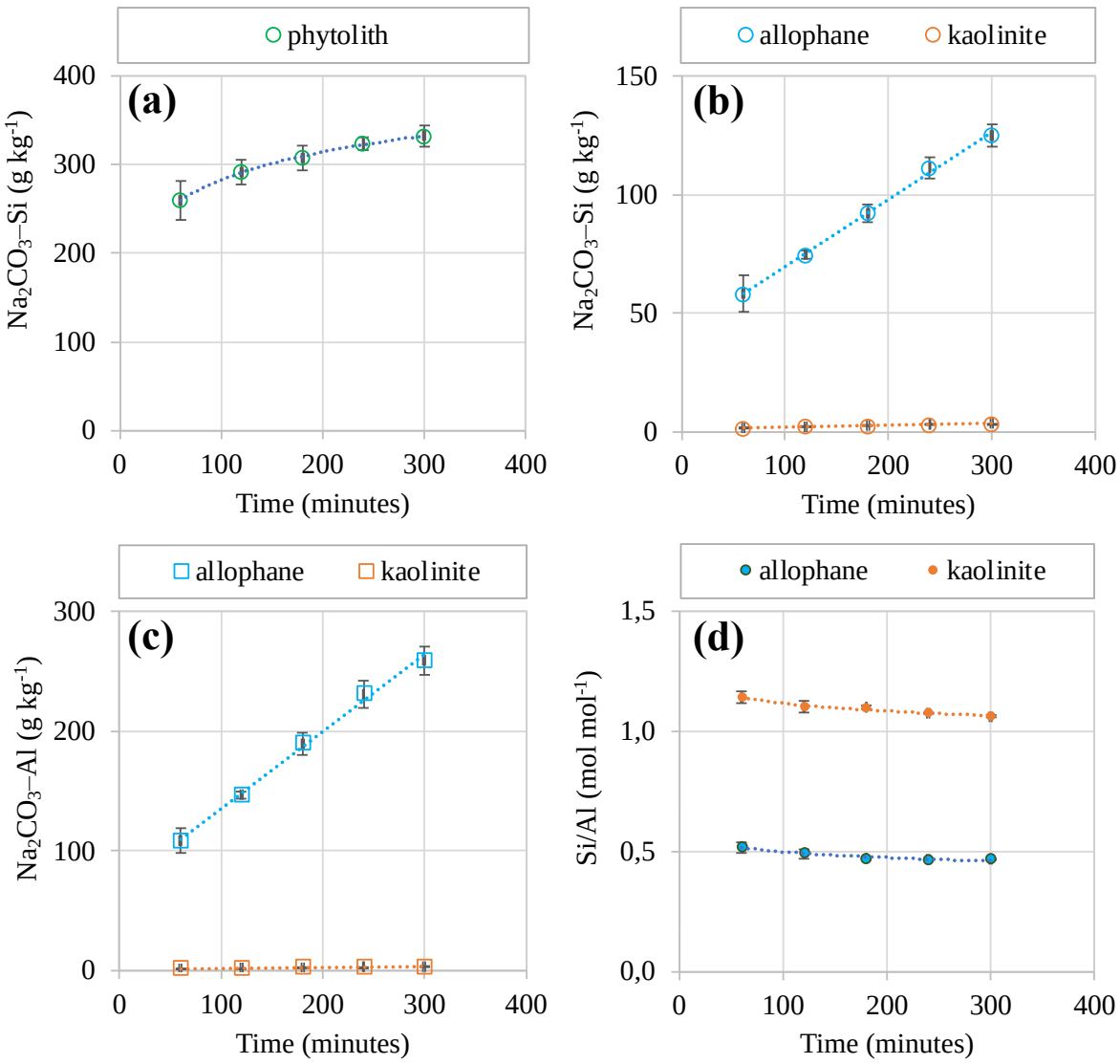

Figure S3. Time evolution of Si and Al concentrations in 0.1 M Na_2CO_3 extracts (Na_2CO_3–Si, Na_2CO_3–Al) from Si bearing phases: Na_2CO_3–Si in (a) rice phytolith, (b) allophane and kaolinite, Na_2CO_3–Al in (c) allophane and kaolinite; Si/Al molar ratio (d) in allophane and kaolinite. Note: Al was not detected in rice phytoliths; both Si and Al were not detected in quartz, organic matter, ferrihydrite and goethite.

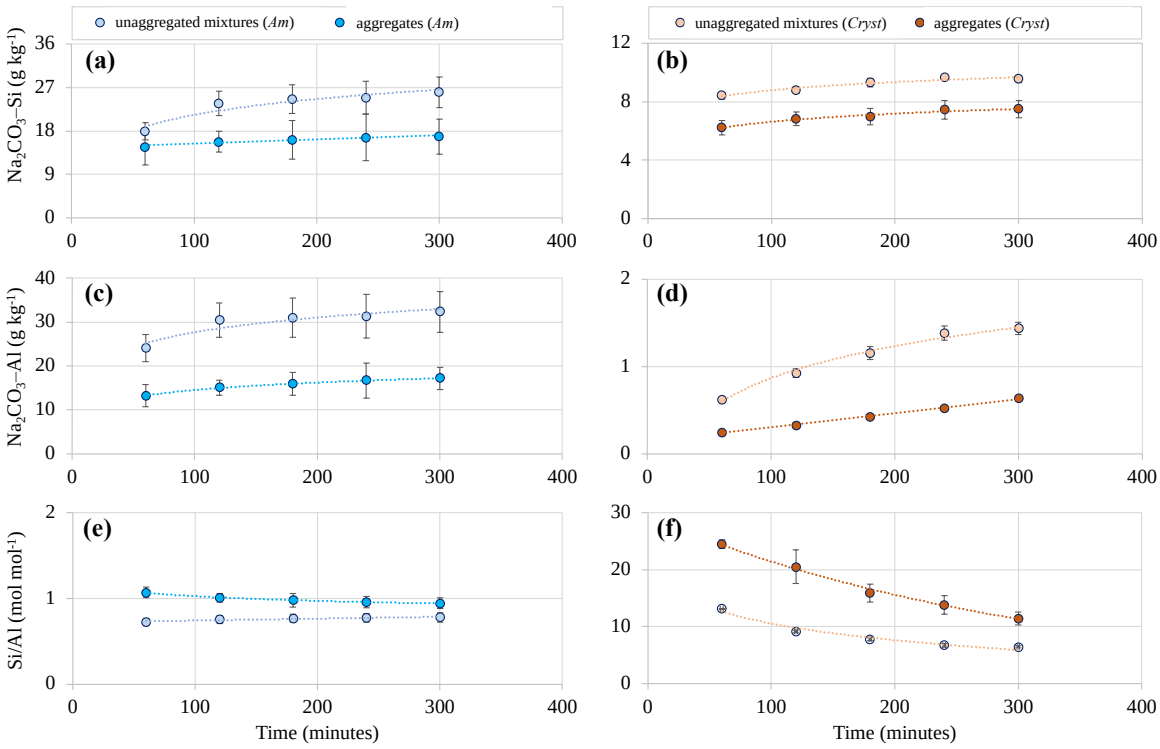

Figure S4. Time evolution of Si and Al concentrations in 0.1 M Na_2CO_3 extracts (Na_2CO_3–Si, Na_2CO_3–Al) and Si/Al molar ratio from unaggregated mixtures and aggregates of (left) the amorphous (*Am*) and (right) crystalline (*Cryst*) models: Na_2CO_3–Si evolution in (a) *Am* model, (b) *Cryst* model, Na_2CO_3–Al evolution in (c) *Am* model, (d) *Cryst* model; Si/Al molar ratio in (e) *Am* model, (f) *Cryst* model.

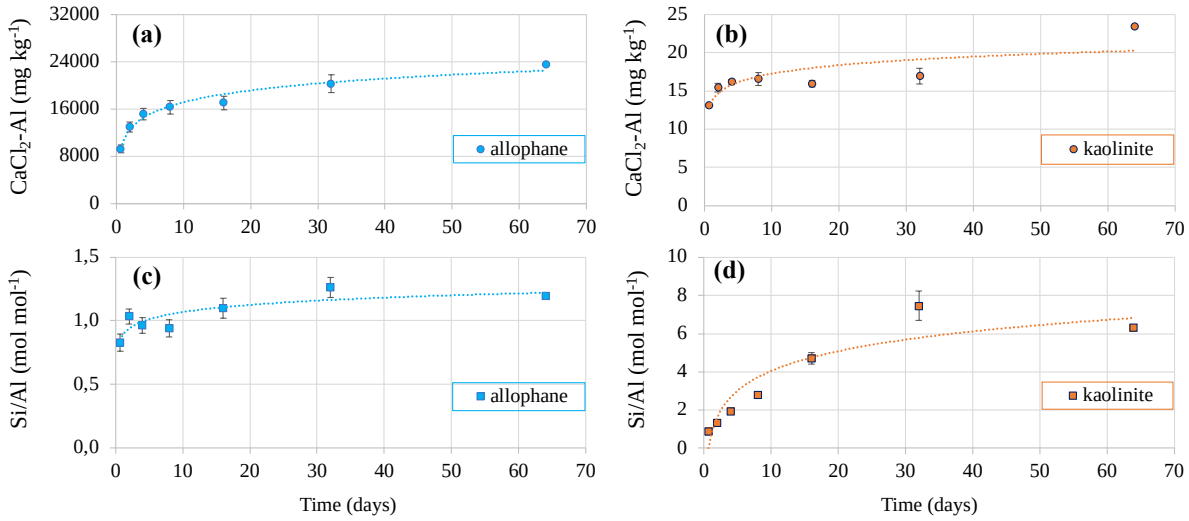

Figure S5. Time evolution of Al concentration in the 0.01 M $CaCl_2$ extract ($CaCl_2$–Al) (a, b), and concomitant Si/Al molar ratio (c, d) for allophane (c) and kaolinite (d), Al being not detected in quartz.

Table S1. Contents of oxalate(o)-extractable Si, Al, Fe and DCB(d)-extractable Fe of allophane, kaolinite, ferrihydrite and goethite.

	Si_o	Al_o	Fe_o	Fe_d	Si_o/Al_o	Fe_o/Fe_d
	g kg^{-1}				mol mol^{-1}	mol mol^{-1}
allophane	109.65	158.15	nd*	nd	0.67	nd
kaolinite	0.26	0.57	0.015	0.017	0.45	0.88
ferrihydrite	nd	nd	528.76	610.67	nd	0.86
goethite	nd	nd	2.72	611.12	nd	0.004

* nd: not detected.

Table S2. pH, concentrations of H_4SiO_4 and Al^{3+} in 0.01 M $CaCl_2$ extracts from 16 hours to 64 days for (a-d) phytolith, quartz, kaolinite, allophane, and for (e-h) mixtures and aggregates of both the amorphous (*Am*) and crystalline (*Cryst*) models.

	days	**16h**	**2**	**4**	**8**	**16**	**32**	**64**
	$\log_{10}(H_4SiO_4)$	-3.14	-2.45	-2.33	-2.26	-2.01	-1.74	-1.72
(a) phytolith	pH	3.59	4.33	3.57	3.68	3.67	3.90	3.56
	$\log_{10}(Al^{3+})$	nd*	nd	Nd	nd	nd	nd	nd
	$\log_{10}(H_4SiO_4)$	-5.20	-4.44	-4.39	-4.19	-4.20	-4.21	-4.16
(b) quartz	pH	5.87	5.82	4.46	4.61	4.67	4.50	4.41
	$\log_{10}(Al^{3+})$	nd	nd	Nd	nd	nd	nd	nd
	$\log_{10}(H_4SiO_4)$	-4.39	-4.13	-3.96	-3.78	-3.57	-3.35	-3.28
(c) kaolinite	pH	3.69	3.54	3.58	3.70	3.75	3.92	3.85
	$\log_{10}(Al^{3+})$	-6.31	-6.24	-6.22	-6.21	-6.23	-6.20	-6.06
	$\log_{10}(H_4SiO_4)$	-1.56	-1.32	-1.29	-1.26	-1.18	-1.04	-1.00
(d) allophane	pH	3.72	3.67	3.94	4.12	4.05	4.07	4.01
	$\log_{10}(Al^{3+})$	-3.46	-3.32	-3.25	-3.22	-3.20	-3.12	-3.06
	$\log_{10}(H_4SiO_4)$	-2.95	-2.69	-2.40	-2.23	-2.07	-1.90	-1.89
(e) unaggregated mixture (*Am*)	pH	4.00	3.78	4.12	4.22	4.36	4.27	4.41
	$\log_{10}(Al^{3+})$	-4.71	-4.50	-4.17	-4.00	-3.84	-3.77	-3.87
	$\log_{10}(H_4SiO_4)$	-3.03	-2.93	-3.01	-2.96	-2.84	-2.70	-2.49
(f) aggregate (*Am*)	pH	3.97	4.18	4.53	4.80	4.71	4.90	4.98
	$\log_{10}(Al^{3+})$	-4.88	-4.72	-4.41	-4.33	-4.31	-4.21	-4.10
	$\log_{10}(H_4SiO_4)$	-3.69	-3.28	-3.11	-2.98	-2.90	-2.82	-2.79
(g) unaggregated mixture (*Cryst*)	pH	5.06	5.51	5.66	5.73	6.05	6.78	7.31
	$\log_{10}(Al^{3+})$	-6.45	-6.37	-7.75	-7.76	-7.69	-7.78	-7.75
	$\log_{10}(H_4SiO_4)$	-3.44	-3.27	-3.12	-3.07	-2.95	-2.86	-2.87
(h) aggregate (*Cryst*)	pH	6.78	7.06	6.90	6.88	6.39	7.19	7.83
	$\log_{10}(Al^{3+})$	-7.98	-7.87	-7.87	-7.87	-7.87	-7.75	-7.78

* nd: not detected.